

A Cartesian grid-based boundary integral method for moving interface problems

Han Zhou^a, Wenjun Ying^{a,*}

^a*School of Mathematical Sciences, MOE-LSC and Institute of Natural Sciences, Shanghai Jiao Tong University, Minhang, Shanghai 200240, PR China*

Abstract

This paper proposes a Cartesian grid-based boundary integral method for efficiently and stably solving two representative moving interface problems, the Hele-Shaw flow and the Stefan problem. Elliptic and parabolic partial differential equations (PDEs) are reformulated into boundary integral equations and are then solved with the matrix-free generalized minimal residual (GMRES) method. The evaluation of boundary integrals is performed by solving equivalent and simple interface problems with finite difference methods, allowing the use of fast PDE solvers, such as fast Fourier transform (FFT) and geometric multigrid methods. The interface curve is evolved utilizing the $\theta - L$ variables instead of the more commonly used $x - y$ variables. This choice simplifies the preservation of mesh quality during the interface evolution. In addition, the $\theta - L$ approach enables the design of efficient and stable time-stepping schemes to remove the stiffness that arises from the curvature term. Ample numerical examples, including simulations of complex viscous fingering and dendritic solidification problems, are presented to showcase the capability of the proposed method to handle challenging moving interface problems.

Keywords: Hele-Shaw flow; The Stefan problem; Cartesian grid; Boundary integral equations; Kernel-free boundary integral method; Small scale decomposition

1. Introduction

Moving interface problems are encountered in various fields of natural sciences and industrial applications, ranging from mathematics [1, 2, 3] and fluid mechanics [4, 5, 6] to material sciences [7, 8, 9, 10] and imaging sciences [11, 12]. In these problems, interfaces are present, dividing the surrounding region into different sub-regions where the underlying physics is governed by PDEs.

When the motion of the interface is not known in advance and needs to be determined as part of solving the entire problem, it is referred to as a free boundary problem. Free boundary problems are inherently nonlinear and pose computational challenges due to the coupling between the dynamics of the interface and the underlying PDEs.

In this paper, we focus on two representative free boundary problems: the Hele-Shaw flow [13, 14, 15] and the Stefan problem [9, 16, 17]. The Hele-Shaw problem describes the flow of

*Corresponding author

Email addresses: zhouhan@sjtu.edu.cn (Han Zhou), wying@sjtu.edu.cn (Wenjun Ying)

Preprint submitted to Elsevier

September 6, 2023

a viscous fluid in a thin gap between two parallel plates and is an elliptic type problem. The Stefan problem, on the other hand, models the solidification or melting of a material with a moving interface and is a parabolic type problem. These problems have been extensively studied in terms of their numerical methods and analysis, due to their significance in applications and the computational difficulties they pose.

Developing accurate and efficient numerical methods for moving interface problems poses several challenges. The first challenge lies in accurately approximating a complex and evolving interface. Although various numerical methods have been developed, such as the front-tracking method [18, 19, 16], the level set method [20, 21, 22, 23, 24], the volume of fluid method [25, 26], and phase-field methods [27, 28, 29], obtaining both simplicity and accuracy in approximations remains challenging. The second challenge is related to solving PDEs on complex and time-varying domains. Due to the evolving interface, methods like the classical finite element method, which relies on body-fitted meshes, require frequent re-meshing procedures to maintain mesh quality. This not only leads to computational inefficiencies but also requires additional implementation efforts. Additionally, conventional boundary integral equation methods [17, 14, 30, 31, 32, 15] are efficient for homogeneous PDEs but have limitations such as the need for dense matrix-vector multiplications and evaluations of singular integrals. In recent decades, Cartesian grid-based methods have gained popularity for moving interface problems. These methods, including the immersed boundary method (IBM) [33, 34, 35], the immersed interface method (IIM) [36, 37, 38, 39], and the ghost fluid method (GFM) [40, 41, 42, 43], involve immersing the moving interface into a fixed background mesh, typically a Cartesian grid. This approach simplifies the algorithm and improves computational efficiency.

When considering the effect of surface tension on the interface, the problem formulation includes the Laplace-Young equation or the Gibbs-Thomson relation to account for local curvature. However, the presence of high-order derivatives in the curvature introduces stiffness into the evolution problem and imposes strict stability constraints on the time step when using explicit time-stepping schemes. Conversely, using a straightforward implicit scheme becomes complicated and computationally expensive due to the nonlinear and nonlocal nature of the interface velocity as a function of the interface position. To address these challenges, Hou et al. developed the small scale decomposition (SSD) method [14]. This method successfully removes stiffness induced by surface tension by employing a special $\theta - L$ formulation of the interface and an implicit discretization for the stiff but linear part of the evolution equation. As a result, the SSD method allows for the application of large time steps, improving computational efficiency. The SSD method has been adapted for solving multiple moving interface problems, including microstructural evolution in inhomogeneous elastic media [44], elastic membranes in viscous flows [45, 46], solid tumor growth [47], and crystal growth [48, 49, 50], among others.

The main objective of this paper is to develop an efficient and stable Cartesian grid-based boundary integral method for solving the Hele-Shaw flow and the Stefan problem. By reformulating the PDEs as boundary integral equations, we use a finite difference analogue of the boundary integral method known as the kernel-free boundary integral (KFBI) method. The KFBI method is based on potential theory and is specifically designed to solve boundary value problems of elliptic equations on irregular domains [51]. It takes advantage of fast PDE solvers on Cartesian grids and eliminates the need to evaluate singular and nearly singular integrals. The method has been extended to higher-order versions and has been successfully applied to solve various problems in the past [52, 53, 54]. To accurately track the moving interface, the $\theta - L$ approach is utilized to represent the Jordan curve and achieve equidistant interface discretization. In addition, the SSD method is employed to enhance the efficiency and stability of numerical

schemes for interface evolutions in both the Hele-Shaw flow and the Stefan problem.

The remainder of this paper is organized as follows: In Section 2, we outline the governing equations of the Hele-Shaw problem and the Stefan problem. Section 3 introduces time discretization methods for time-dependent PDEs and formulations of boundary integral equations. The kernel-free boundary integral method is elaborated upon in Section 4. Numerical approaches for interface evolution are described in Section 5. Numerical results are presented in Section 6. Finally, in Section 7, we briefly discuss the advantages of the proposed method and potential areas for improvement.

2. Moving interface problems

Let $\Gamma : [0, 2\pi) \times [0, T] \rightarrow \mathbb{R}^2$ be a time-dependent and closed curve separating a domain $\mathcal{U} \subset \mathbb{R}^2$ into an interior domain Ω^+ and an exterior domain Ω^- . Generally, the domain \mathcal{U} can be bounded or unbounded. We shall assume that the interior domain Ω^+ is bounded and can be covered by a bounding box \mathcal{B} , see Fig 1. In moving interface problems, the physical quantities defined in Ω^+ and Ω^- satisfy certain PDEs. Interface or boundary conditions are also prescribed on the moving interface Γ for the PDEs.

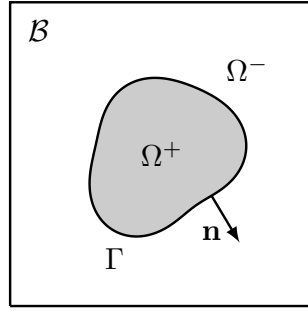


Figure 1: A Schematic of a moving interface problem.

2.1. The Hele-Shaw flow

We consider an exterior moving interface problem of the Hele-Shaw flow that describes the motion of an air bubble in a radial Hele-Shaw cell. The moving interface Γ separates the full space \mathbb{R}^2 into an air domain Ω^+ and an oil domain Ω^- . In the air domain, the pressure is assumed to be constant, which we may take to be zero. In the oil domain, the fluid velocity \mathbf{u} and pressure p satisfy Darcy's law, together with the incompressibility constraint:

$$\mathbf{u} = -M\nabla p, \quad \nabla \cdot \mathbf{u} = 0, \quad \text{in } \Omega^-, \quad (1)$$

where $M = \frac{b^2}{12\mu}$ is the mobility of the fluid, b is the gap width of the Hele-Shaw cell, and μ is the viscosity. Consider constant injection of air at the origin,

$$\nabla \cdot \mathbf{u} = 2\pi J\delta(\mathbf{x}), \quad \text{in } \Omega^-, \quad (2)$$

where $J \geq 0$ is a constant injection rate and δ is the Dirac delta function modeling the air injection. Combining equations (1) and (2), and assuming $M = 1$, we obtain the Poisson equation for the pressure

$$\Delta p = -2\pi J\delta(\mathbf{x}), \quad \text{in } \Omega^-. \quad (3)$$

Although the Dirac delta function in the right-hand side of (3) vanishes in Ω^- , it prescribes the behavior of the solution at infinity $p = -J \ln |\mathbf{x}| + C + o(1)$ as $|\mathbf{x}| \rightarrow \infty$, where C is a constant ambient pressure. On the moving interface Γ , the pressure is given by the Laplace-Young condition

$$p = -\sigma\kappa, \quad \text{on } \Gamma, \quad (4)$$

where $\sigma > 0$ is the surface tension coefficient and κ is the local curvature of Γ . In addition, the motion of the moving interface Γ follows the kinematic condition

$$\frac{d\mathbf{x}}{dt} = \mathbf{u}, \quad \text{for } \mathbf{x} \in \Gamma. \quad (5)$$

As a matter of fact, since we are only interested in the shape of Γ , it suffices only to prescribe the normal velocity V_n ,

$$V_n = \frac{d\mathbf{x}}{dt} \cdot \mathbf{n} = \mathbf{u} \cdot \mathbf{n} = -\partial_{\mathbf{n}} p, \quad \text{for } \mathbf{x} \in \Gamma. \quad (6)$$

where \mathbf{n} is the unit outward normal of Γ .

2.2. The Stefan problem

We also consider the Stefan problem that models diffusion-driven phase changes between solid and liquid phases. Here, the moving solid-liquid interface Γ separates the box domain \mathcal{B} into the solid region Ω^+ and the liquid region Ω^- . In the classical Stefan problem, the temperature field T satisfies the heat equation in both solid and liquid regions,

$$\partial_t T = \Delta T, \quad \text{in } \Omega^+ \cup \Omega^-. \quad (7)$$

On the solid-liquid interface, the temperature is continuous and is coupled with the surface tension and the molecular kinematic effect through the Gibbs-Thomson relation

$$T + \varepsilon_C(\mathbf{n})\kappa + \varepsilon_V(\mathbf{n})V_n = 0, \quad \text{on } \Gamma, \quad (8)$$

where $\varepsilon_C(\mathbf{n})$ and $\varepsilon_V(\mathbf{n})$ are surface tension and molecular kinetic coefficients, which are non-negative and may depend on the orientation of the interface. The normal velocity of Γ is determined by the Stefan equation.

$$V_n = [\partial_{\mathbf{n}} T]. \quad (9)$$

Here, the notation $[\cdot]$ means the jump value of a quantity across the interface. For example, given a piece-wise continuous function q , we have

$$[q](\mathbf{x}) = q^+(\mathbf{x}) - q^-(\mathbf{x}) = \lim_{\mathbf{y} \in \Omega^+, \mathbf{y} \rightarrow \mathbf{x}} q(\mathbf{y}) - \lim_{\mathbf{y} \in \Omega^-, \mathbf{y} \rightarrow \mathbf{x}} q(\mathbf{y}), \quad \text{for } \mathbf{x} \in \Gamma. \quad (10)$$

A suitable boundary condition should also be prescribed on the outer boundary $\partial\mathcal{B}$, for which we choose a no-flux boundary condition $\partial_{\mathbf{n}} T = 0$. For modeling solidification problems, initially, a solid seed is placed in an undercooled surrounding liquid. The temperature in the solid seed is assumed to be equal to the melt temperature T_m , and the temperature in the undercooled liquid is given by T_∞ . The degree of undercooling is described by the Stefan number $St = T_\infty - T_m$.

In a more general setting, the temperature differences in the liquid phase lead to changes in the specific volume of fluid parcels and, hence, the fluid density. The density changes further

lead to buoyancy force-driven convection of the fluid. With the Boussinesq approximation [55], we assume the fluid is incompressible, and the effect of density changes only appears in the buoyancy force. Incorporating the natural convection effect, the Stefan problem is governed by the following system

$$\partial_t T = \Delta T, \quad \text{in } \Omega^+, \quad (11)$$

$$\partial_t T + \mathbf{u} \cdot \nabla T = \Delta T, \quad \text{in } \Omega^-, \quad (12)$$

$$\partial_t \mathbf{u} + (\mathbf{u} \cdot \nabla) \mathbf{u} = \Delta \mathbf{u} - \nabla p + \mathbf{G}, \quad \text{in } \Omega^-, \quad (13)$$

$$\nabla \cdot \mathbf{u} = 0, \quad \text{in } \Omega^-, \quad (14)$$

where \mathbf{u} is fluid velocity, p is pressure. Here, we have assumed that the density and viscosity of the fluid are 1. The buoyancy force \mathbf{G} under the Boussinesq approximation is linearly proportional to the temperature difference,

$$\mathbf{G} = -g\beta(T - T_\infty)\mathbf{j}, \quad (15)$$

where g represents the gravity acceleration, β denotes the thermal expansion coefficient, \mathbf{j} denotes the unit vector in the vertical direction. On the solid-liquid interface Γ , the Gibbs-Thomson relation (8) and the Stefan equation (9) are given for the temperature field, and the no-slip boundary condition is specified for the fluid. On the outer boundary $\partial\mathcal{B}$, we set $\partial_{\mathbf{n}}T = 0$ and $\mathbf{u} = \mathbf{u}_b$ where \mathbf{u}_b is the boundary data describing in/out-flow or no-slip boundary conditions. It is worth mentioning that the model is a two-way coupling of the temperature and the velocity field through the fluid convection and buoyancy force.

3. Time discretization and boundary integral equations

The PDEs in the last section are all solved in a boundary integral equation framework. Time-dependent parabolic PDEs are discretized in time to obtain a sequence of elliptic PDEs, for which we can formulate equivalent boundary integral equations. Let $t_n = n\tau$, $n = 0, 1, \dots, N_T$ be the uniform temporal mesh where $\tau = T/N_T$ is the time step. For a function f , denote by f^n the numerical approximation of $f(t_n)$.

3.1. The Hele-Shaw flow

In the Hele-Shaw flow, the solution to the Poisson equation (3) with the boundary condition (4) can be represented as the sum of two functions v and w , where

$$v(\mathbf{x}) = -J \ln |\mathbf{x}|. \quad (16)$$

comes from the point-source term and $w(\mathbf{x})$ satisfies the exterior problem of the Laplace equation

$$\Delta w = 0, \quad \text{in } \Omega^-, \quad (17)$$

$$w = -\sigma\kappa - v, \quad \text{on } \Gamma. \quad (18)$$

Let $G_0(\mathbf{y}, \mathbf{x}) = (1/2\pi) \ln |\mathbf{y} - \mathbf{x}|$ be the free-space Green function associated with the Laplacian Δ , the solution $w(\mathbf{x})$ can be represented as a modified double-layer potential

$$w(\mathbf{x}) = (D\varphi)(\mathbf{x}) + \int_{\Gamma} \varphi(\mathbf{y}) d\mathbf{s}_y = \int_{\Gamma} \varphi(\mathbf{y}) \left(\frac{\partial G_0(\mathbf{y}, \mathbf{x})}{\partial \mathbf{n}_y} + 1 \right) d\mathbf{s}_y, \quad (19)$$

where φ is an unknown dipole density function defined on Γ . The boundary integral formulation of w naturally matches the boundary condition at infinity. Restricting (19) on Γ and using the boundary condition (18), we obtain a boundary integral equation for the density function φ ,

$$-\frac{1}{2}\varphi(\mathbf{x}) + \int_{\Gamma} \varphi(\mathbf{y}) \left(\frac{\partial G_0(\mathbf{y}, \mathbf{x})}{\partial \mathbf{n}_y} + 1 \right) d\mathbf{s}_y = -\sigma\kappa - v(\mathbf{x}), \quad \text{for } \mathbf{x} \in \Gamma. \quad (20)$$

The boundary integral equation is a Fredholm integral equation of the second kind and is well-conditioned.

3.2. The classical Stefan problem

We first discretize the time-dependent heat equation in time to reduce the problem into solving an elliptic equation in each time step. For better accuracy and stability, the second-order backward differentiation formula (BDF2) is employed for the time discretization

$$\frac{3T^{n+1} - 4T^n + T^{n-1}}{2\tau} = \Delta T^{n+1}, \quad \text{in } \Omega^+ \cup \Omega^-. \quad (21)$$

It leads to a modified Helmholtz equation for T^{n+1}

$$\left(\Delta - \frac{3}{2\tau} \right) T^{n+1} = \frac{T^{n-1} - 4T^n}{2\tau}, \quad \text{in } \Omega^+ \cup \Omega^-, \quad (22)$$

The modified Helmholtz equation is also subject to jump conditions $[T^{n+1}] = 0$ and $[\partial_{\mathbf{n}} T^{n+1}] = V_n$ on Γ and an outer boundary condition $\partial_{\mathbf{n}} T^{n+1} = 0$ on $\partial\mathcal{B}$. Let $c = \sqrt{3/(2\tau)}$. We split T^{n+1} into two parts $T^{n+1} = T_1 + T_2$, where T_1 is the solution to the modified Helmholtz equation with an inhomogeneous right-hand side,

$$\Delta T_1 - c^2 T_1 = \frac{T^{n-1} - 4T^n}{2\tau}, \quad \text{in } \mathcal{B}, \quad (23)$$

$$\partial_{\mathbf{n}} T_1 = 0, \quad \text{on } \partial\mathcal{B}, \quad (24)$$

and T_2 is the solution to the interface problem with a homogeneous right-hand side,

$$\Delta T_2 - c^2 T_2 = 0, \quad \text{in } \Omega^+ \cup \Omega^-, \quad (25)$$

$$[T_2] = 0, \quad \text{on } \Gamma, \quad (26)$$

$$[\partial_{\mathbf{n}} T_2] = V_n, \quad \text{on } \Gamma, \quad (27)$$

$$\partial_{\mathbf{n}} T_2 = 0, \quad \text{on } \partial\mathcal{B}. \quad (28)$$

Since the temperature field T is continuous across the interface Γ , the right-hand side of (23) is also continuous. Therefore, the part T_1 is much more regular than T_2 , and the problem (23) and (24) can be solved with a standard finite difference method. For each fixed $\mathbf{x} \in \mathcal{B}$, let $G_c(\mathbf{y}, \mathbf{x})$ be the Green function that satisfies

$$(\Delta - c^2)G_c(\mathbf{y}, \mathbf{x}) = \delta(\mathbf{y} - \mathbf{x}), \quad \text{for } \mathbf{y} \in \mathcal{B}, \quad (29)$$

$$\partial_{\mathbf{n}} G_c(\mathbf{y}, \mathbf{x}) = 0, \quad \text{for } \mathbf{y} \in \partial\mathcal{B}. \quad (30)$$

The part T_2 can be expressed as a single layer potential

$$T_2(\mathbf{x}) = -(S\psi)(\mathbf{x}) = - \int_{\Gamma} G_c(\mathbf{y}, \mathbf{x})\psi(\mathbf{y}) d\mathbf{s}_y, \quad \text{for } \mathbf{x} \in \mathcal{B}. \quad (31)$$

where ψ is an unknown density function defined on Γ . Note that we also have $\psi = [\partial_n T_2] = V_n$. Further, with the Gibbs-Thomson relation (8), a boundary integral equation can be obtained for the density function ψ ,

$$\varepsilon_V \psi(\mathbf{x}) - \int_{\Gamma} G_c(\mathbf{y}, \mathbf{x})\psi(\mathbf{y}) d\mathbf{s}_y = -\varepsilon_C \kappa(\mathbf{x}) - T_1(\mathbf{x}), \quad \text{for } \mathbf{x} \in \Gamma. \quad (32)$$

For a nonzero ε_V , the boundary integral equation (32) is a Fredholm integral equation of the second kind. It degenerates to a first-kind Fredholm integral equation if ε_V vanishes.

3.3. The Stefan problem with natural convection

Similar to the heat equation, we first discretize time derivatives in the time-dependent advection-diffusion equation (12) and the Navier-Stokes equation (13), (14), and reduce the problems into elliptic equations in each time step. To avoid treating the nonlinear advection term, we advance T, \mathbf{u}, p with a semi-Lagrangian method in time. In the semi-Lagrangian discretization, the advection terms are incorporated into material derivatives, namely,

$$\frac{dT}{dt} = \Delta T, \quad \text{in } \Omega^+ \cup \Omega^-, \quad (33)$$

$$\frac{d\mathbf{u}}{dt} = \Delta \mathbf{u} - \nabla p + \mathbf{G}, \quad \text{in } \Omega^-, \quad (34)$$

$$\nabla \cdot \mathbf{u} = 0, \quad \text{in } \Omega^-, \quad (35)$$

where $\frac{d}{dt} = \partial_t + \mathbf{u} \cdot \nabla$ is the material derivative. Here, we assume \mathbf{u} equals zero in the solid domain, so the temperature in both domains satisfies the same equation (33). A second-order semi-implicit is used to discretize equations (33) to (35),

$$\frac{3T^{n+1} - 4\tilde{T}^n + \tilde{T}^{n-1}}{2\tau} = \Delta T^{n+1}, \quad \text{in } \Omega^+ \cup \Omega^-, \quad (36)$$

$$\frac{3\mathbf{u}^{n+1} - 4\tilde{\mathbf{u}}^n + \tilde{\mathbf{u}}^{n-1}}{2\tau} = \Delta \mathbf{u}^{n+1} - \nabla p^{n+1} + 2\mathbf{G}^n - \mathbf{G}^{n-1}, \quad \text{in } \Omega^-, \quad (37)$$

$$\nabla \cdot \mathbf{u}^{n+1} = 0, \quad \text{in } \Omega^-. \quad (38)$$

where $\tilde{\mathbf{u}}^n, \tilde{T}^n, \tilde{\mathbf{u}}^{n-1}$, and \tilde{T}^{n-1} are the fluid velocities and temperatures at the departure points \mathbf{x}^n and \mathbf{x}^{n-1} , respectively. The scheme treats the buoyancy term explicitly such that the resulting discrete system is not coupled and can be solved separately. The departure points \mathbf{x}^n and \mathbf{x}^{n-1} can be found by solving the initial value problem backward in time,

$$\frac{d\mathbf{x}(t)}{dt} = \mathbf{u}(\mathbf{x}(t), t), \quad \mathbf{x}(t_{n+1}) = \mathbf{x}_0. \quad (39)$$

A second-order mid-point method is used for computing the positions of the departure points,

$$\mathbf{x}^* = \mathbf{x}_0 - \frac{\tau}{2} \mathbf{u} \left(\mathbf{x}_0 - \frac{\tau}{2} \mathbf{u}^{n+\frac{1}{2}}, t_{n+\frac{1}{2}} \right), \quad \mathbf{x}^n = \mathbf{x}_0 - \tau \mathbf{u} \left(\mathbf{x}^*, t_{n+\frac{1}{2}} \right), \quad (40)$$

$$\mathbf{x}^* = \mathbf{x}_0 - \tau \mathbf{u} \left(\mathbf{x}_0 - \tau \mathbf{u}^n, t_n \right), \quad \mathbf{x}^{n-1} = \mathbf{x}_0 - 2\tau \mathbf{u} \left(\mathbf{x}^*, t_n \right). \quad (41)$$

Off-grid values of \mathbf{u} are computed with the cubic Lagrangian interpolation and the velocity at $t_{n+\frac{1}{2}}$ is computed with a second-order extrapolation scheme $\mathbf{u}^{n+\frac{1}{2}} = \frac{3}{2}\mathbf{u}^n - \frac{1}{2}\mathbf{u}^{n-1}$. After making some rearrangements, we arrive at the modified Helmholtz equation

$$\left(\Delta - \frac{3}{2\tau}\right)T^{n+1} = \frac{\tilde{T}^{n-1} - 4\tilde{T}^n}{2\tau}, \quad \text{in } \Omega^+ \cup \Omega^-, \quad (42)$$

subject to interface and boundary conditions on Γ and $\partial\mathcal{B}$ as mentioned before, and the modified Stokes equation

$$\left(\Delta - \frac{3}{2\tau}\right)\mathbf{u}^{n+1} - \nabla p^{n+1} = \frac{\tilde{\mathbf{u}}^{n-1} - 4\tilde{\mathbf{u}}^n}{2\tau} + 2\mathbf{G}^n - \mathbf{G}^{n-1}, \quad \text{in } \Omega^-, \quad (43a)$$

$$\nabla \cdot \mathbf{u}^{n+1} = 0, \quad \text{in } \Omega^-, \quad (43b)$$

subject to boundary conditions

$$\mathbf{u}^{n+1} = \mathbf{0}, \quad \text{on } \Gamma, \quad \mathbf{u}^{n+1} = \mathbf{u}_b, \quad \text{on } \partial\mathcal{B}, \quad (44)$$

The boundary integral formulation for the modified Helmholtz (42) is similar to that for (22), and we omit it. We shall give the boundary integral equation for the modified Stokes (43). We split the solution pair into two parts $(\mathbf{u}^{n+1}, p^{n+1}) = (\mathbf{u}_1, p_1) + (\mathbf{u}_2, p_2)$. The particular solution (\mathbf{u}_1, p_1) satisfies the modified Stokes equation with an inhomogeneous right-hand side

$$(\Delta - c^2)\mathbf{u}_1 - \nabla p_1 = \mathbf{f}, \quad \text{in } \mathcal{B}, \quad (45a)$$

$$\nabla \cdot \mathbf{u}_1 = 0, \quad \text{in } \mathcal{B}, \quad (45b)$$

$$\mathbf{u}_1 = \mathbf{u}_b, \quad \text{on } \partial\mathcal{B}, \quad (45c)$$

where $c = \sqrt{3/(2\tau)}$ and \mathbf{f} is given by

$$\mathbf{f} = \begin{cases} \frac{\tilde{\mathbf{u}}^{n-1} - 4\tilde{\mathbf{u}}^n}{2\tau} + 2\mathbf{G}^n - \mathbf{G}^{n-1}, & \text{in } \Omega^-, \\ 2\mathbf{G}^n - \mathbf{G}^{n-1}, & \text{in } \Omega^+. \end{cases} \quad (46)$$

Note that \mathbf{f} is a continuous extension of the right-hand side of (43a) due to the no-slip boundary condition on Γ . Then the part (\mathbf{u}_1, p_1) has high regularity, and standard finite difference methods for the Stokes equation can be applied. The second part (\mathbf{u}_2, p_2) satisfies an exterior Dirichlet boundary value problem

$$(\Delta - c^2)\mathbf{u}_2 - \nabla p_2 = \mathbf{0}, \quad \text{in } \Omega^-, \quad (47)$$

$$\nabla \cdot \mathbf{u}_2 = 0, \quad \text{in } \Omega^-, \quad (48)$$

$$\mathbf{u}_2 = -\mathbf{u}_1, \quad \text{on } \Gamma, \quad (49)$$

$$\mathbf{u}_2 = \mathbf{0}, \quad \text{on } \partial\mathcal{B}. \quad (50)$$

For each fixed $\mathbf{x} \in \mathcal{B}$, let $(\mathbf{G}_u(\mathbf{y}, \mathbf{x}), \mathbf{G}_p(\mathbf{y}, \mathbf{x}))$ be the Green function pair that satisfies

$$(\Delta - c^2)\mathbf{G}_u(\mathbf{y}, \mathbf{x}) - \nabla \mathbf{G}_p(\mathbf{y}, \mathbf{x}) = \delta(\mathbf{y} - \mathbf{x})\mathbf{I}, \quad \text{for } \mathbf{y} \in \mathcal{B}, \quad (51)$$

$$\nabla \cdot \mathbf{G}_p(\mathbf{y}, \mathbf{x}) = 0, \quad \text{for } \mathbf{y} \in \mathcal{B}, \quad (52)$$

$$\mathbf{G}_u(\mathbf{y}, \mathbf{x}) = \mathbf{0}, \quad \text{for } \mathbf{y} \in \partial\mathcal{B}. \quad (53)$$

Then the solution pair (\mathbf{u}_2, p_2) can be represented as a double-layer potential $D\boldsymbol{\varphi} = (D_{\mathbf{u}}\boldsymbol{\varphi}, D_p\boldsymbol{\varphi})^T$ [56],

$$\mathbf{u}_2(\mathbf{x}) = (D_{\mathbf{u}}\boldsymbol{\varphi})(\mathbf{x}) = \int_{\Gamma} T(\mathbf{G}_{\mathbf{u}}, \mathbf{G}_p)(\mathbf{y}, \mathbf{x})\boldsymbol{\varphi}(\mathbf{y}) ds_{\mathbf{y}}, \quad (54)$$

$$p_2(\mathbf{x}) = (D_p\boldsymbol{\varphi})(\mathbf{x}) = 2 \int_{\Gamma} \frac{\partial \mathbf{G}_p(\mathbf{y}, \mathbf{x})}{\partial \mathbf{n}_{\mathbf{y}}} \boldsymbol{\varphi}(\mathbf{y}) ds_{\mathbf{y}}. \quad (55)$$

where $\boldsymbol{\varphi} = (\varphi_1, \varphi_2)^T$ is a vector-valued unknown density function defined on Γ and $T(\mathbf{u}, p) = -p\mathbf{n} + (\nabla\mathbf{u} + \nabla\mathbf{u}^T)\mathbf{n}$ is the traction operator. Restricting (54) to Γ leads to the boundary integral equation

$$-\frac{1}{2}\boldsymbol{\varphi}(\mathbf{x}) + \int_{\Gamma} T(\mathbf{G}_{\mathbf{u}}, \mathbf{G}_p)(\mathbf{y}, \mathbf{x})\boldsymbol{\varphi}(\mathbf{y}) ds_{\mathbf{y}} = -\mathbf{u}_1(\mathbf{x}), \quad \text{for } \mathbf{x} \in \Gamma. \quad (56)$$

The boundary integral equation is also a Fredholm integral equation of the second kind and is well-conditioned.

4. Kernel-free boundary integral method

The boundary integral equations (20), (32) and (56) are solved with the kernel-free boundary integral method. The discrete systems of boundary integral equations are solved with a Krylov subspace iterative method, the GMRES method [57]. In each iteration, one only needs to compute the matrix-vector multiplication operation, which mainly consists of evaluations of boundary integrals. The procedure can be implemented in a matrix-free manner to avoid forming the full matrix. The main idea of the KFBI method is to make use of a Cartesian grid-based PDE solver instead of numerical quadratures for evaluating the boundary integrals.

4.1. Equivalent interface problems

Let \mathcal{A} be an elliptic differential operator that can be the Laplacian, modified Helmholtz, or modified Stokes operator. The evaluation of boundary integral operators associated with \mathcal{A} can be described in the same framework. According to the classical potential theory, the single-layer potential $S\boldsymbol{\psi}(\mathbf{x})$ and the double-layer potential $D\boldsymbol{\varphi}(\mathbf{x})$ satisfy equivalent interface problems [56, 51], which can be unified as

$$\begin{cases} \mathcal{A}\mathbf{v} = \mathbf{0}, & \text{in } \Omega^+ \cup \Omega^-, \\ [\boldsymbol{\pi}_D(\mathbf{v})] = \boldsymbol{\Phi}, & \text{on } \Gamma, \\ [\boldsymbol{\pi}_N(\mathbf{v})] = \boldsymbol{\Psi}, & \text{on } \Gamma, \\ \text{some suitable BCs,} & \partial\mathcal{B}. \end{cases} \quad (57)$$

where $(\boldsymbol{\pi}_D, \boldsymbol{\pi}_N)$ is the Cauchy data pair and is specified in (1). The functions $\boldsymbol{\Phi}$ and $\boldsymbol{\Psi}$ are given

Table 1: Cauchy data pair for different elliptic differential operators.

	\mathbf{v}	$\boldsymbol{\pi}_D(\mathbf{v})$	$\boldsymbol{\pi}_N(\mathbf{v})$
$\mathcal{A} = \Delta - c^2$	u	u	$\partial_{\mathbf{n}}u$
$\mathcal{A} = ((\Delta - c^2)\mathbf{I} - \nabla, \nabla \cdot)^T$	$(\mathbf{u}, p)^T$	\mathbf{u}	$T(\mathbf{u}, p)$

Table 2: Jump relations of the single- and double-layer potentials.

	Φ	Ψ
$\mathbf{v} = S\psi$	$\mathbf{0}$	$-\psi$
$\mathbf{v} = D\varphi$	φ	$\mathbf{0}$

in (2). The boundary condition on $\partial\mathcal{B}$ depends on which Green's function is used. For the Hele-Shaw flow, since the problem is defined on an unbounded domain and the box boundary $\partial\mathcal{B}$ is only an artificial boundary. A natural choice is to directly use the potential value on $\partial\mathcal{B}$ as a Dirichlet-type boundary condition. The integral form boundary condition is discretized with the composite trapezoidal rule. Due to the periodicity of the integrand function on Γ , the composite trapezoidal rule is highly accurate. No singular or nearly singular integral needs to be handled here since the quadrature points are on Γ and target points are on $\partial\mathcal{B}$. In the Stefan problem, boundary conditions for the temperature or the fluid field are of Dirichlet or Neumann-type, depending on the problem at hand.

The equivalent interface problem (57) is much simpler than the original problems since the interface condition can be easily decoupled into derivative jumps in each direction, which is shown in Appendix A. After solving the interface problem (57) on a Cartesian grid with an efficient PDE solver, boundary integral values, as well as their normal derivatives, can be extracted from grid values with an interpolation procedure.

We stress that the analytical expression of Green's function is only used in the Hele-Shaw flow to convert the infinite boundary condition to a bounded one. In other cases, the method is kernel-free in the sense that there is no need to use any of Green's functions explicitly. In all cases, evaluations of singular or nearly singular integrals are avoided. Accelerated by fast PDE solvers, the computation of boundary integrals with the KFBI method is efficient and is comparable with the fast multipole method [52].

4.2. Corrected finite difference scheme

The interface problem (57) is solved with a finite difference method with additional corrections near the interface. For simplicity, suppose the computational domain \mathcal{B} is a unit square $[0, 1]^2$ and is uniformly partitioned into N intervals in each spatial direction. The grid nodes are denoted as (x_i, y_j) , $x_i = ih$, $y_j = jh$, $i, j = 0, \dots, N$ where $h = 1/N$ is the mesh size.

4.2.1. The modified Helmholtz equation

Denote by $u_{i,j}$ the numerical approximation of $u(x_i, y_j)$. A standard second-order five-point central difference scheme for the modified Helmholtz equation is given by

$$\Delta_h u_{i,j} - c^2 u_{i,j} = \frac{u_{i+1,j} + u_{i-1,j} + u_{i,j+1} + u_{i,j-1} - 4u_{i,j}}{h^2} - c^2 u_{i,j} = 0. \quad (58)$$

A grid node (x_i, y_j) is called an irregular node if at least one of the stencil nodes is on the other side of the interface. Clearly, irregular nodes are always in the vicinity of Γ . Since the solution has certain jumps on the interface Γ , the local truncation error at an irregular node is on the order of $\mathcal{O}(h^{-2})$ and is too large to achieve an accurate approximation. To show this, we assume at an irregular node $(x_i, y_j) \in \Omega^+$, a stencil node $(x_{i+1}, y_j) \in \Omega^-$ is on the different side of Γ and other stencil nodes are all in Ω^+ . Suppose the interface Γ intersects the grid lines segment between

(x_i, y_j) and (x_{i+1}, y_j) at (ξ, y_j) . By Taylor expansion, the local truncation error at (x_i, y_j) is given by

$$E_h(x_i, y_j) = (\Delta_h - c^2)u(x_i, y_j) = -\frac{1}{h^2}\{[u] + (x_{i+1} - \xi)[u_x] + \frac{1}{2}(x_{i+1} - \xi)^2[u_{xx}]\} + O(h). \quad (59)$$

To avoid the large local truncation error, one can use the leading term as a correction term to the right-hand side of (58). It gives the corrected scheme

$$\Delta_h u_{i,j} - c^2 u_{i,j} = C_{i,j} = -\frac{1}{h^2}\{[u] + (x_{i+1} - \xi)[u_x] + \frac{1}{2}(x_{i+1} - \xi)^2[u_{xx}]\}. \quad (60)$$

The resulting local truncation error becomes $O(h)$. Here, the correction term $C_{i,j}$ is from the contribution of the intersection point (ξ, y_j) and is a linear combination of jump values $[u]$, $[u_x]$, and $[u_{yy}]$, which are known before solving the interface problem, see Appendix A. Similarly, one can derive correction terms for different intersection patterns by Taylor expansions. Evidently, $C_{i,j}$ is non-zero only at irregular nodes and is always a linear combination of the jump values $[u]$, $[u_x]$, $[u_y]$, \dots .

Since irregular nodes are near the interface Γ , which has co-dimension one, the overall accuracy can still be second-order [58]. The correction terms only appear on the right-hand side and the coefficient matrix is not altered, FFT-based fast Poisson solvers can be applied to solve the resulting linear system efficiently.

4.2.2. The modified Stokes equation

The discretization of the modified Stokes equations is based on the marker and cell (MAC) scheme on a staggered grid. The pressure is at the cell center, the x-component of the velocity is at the center of the east and west edges of a cell, and the y-component of the velocity is at the center of the north and south edges of a cell. The discrete mesh functions $u_{i,j}$, $v_{i,j}$, $p_{i,j}$ are defined as

$$u_{i,j} = u(x_i, y_j - h/2), \quad i = 0, 1 \dots, N_x, \quad j = 1, 2 \dots, N_y, \quad (61)$$

$$v_{i,j} = v(x_i - h/2, y_j), \quad i = 1, 2 \dots, N_x, \quad j = 0, 1 \dots, N_y, \quad (62)$$

$$p_{i,j} = p(x_i - h/2, y_j - h/2), \quad i = 1, 2 \dots, N_x, \quad j = 1, 2 \dots, N_y. \quad (63)$$

The MAC scheme for the modified Stokes equation is given by

$$(\Delta_h - c^2)\mathbf{u}_{i,j} - \nabla_h p_{i,j} = \mathbf{0}, \quad (64a)$$

$$\nabla_h \cdot \mathbf{u} = 0, \quad (64b)$$

where Δ_h, ∇_h are the discrete approximations for Δ, ∇ , respectively,

$$\Delta_h \mathbf{u}_{i,j} = \frac{\mathbf{u}_{i+1,j} + \mathbf{u}_{i-1,j} + \mathbf{u}_{i,j+1} + \mathbf{u}_{i,j-1} - 4\mathbf{u}_{i,j}}{h^2}, \quad (65)$$

$$\nabla_h p_{i,j} = \left(\frac{p_{i+1,j} - p_{i,j}}{h}, \frac{p_{i,j+1} - p_{i,j}}{h} \right)^T, \quad (66)$$

$$\nabla_h \cdot \mathbf{u}_{i,j} = \frac{u_{i,j} - u_{i-1,j}}{h} + \frac{v_{i,j} - v_{i,j-1}}{h}. \quad (67)$$

The Dirichlet boundary condition is discretized with a symmetric approach for the x-component velocity on the top and bottom boundary and the y-component velocity on the right and left

boundary. In the presence of interfaces, one can also derive local truncation errors at irregular nodes for each finite difference equation in (64). Similarly, by using the leading term in the local truncation error as a correction term of the right-hand side in (64), we arrived at the corrected MAC scheme

$$(\Delta_h - c^2)\mathbf{u}_{i,j} - \nabla_h p_{i,j} = \mathbf{C}_{i,j}, \quad (68a)$$

$$\nabla_h \cdot \mathbf{u} = D_{i,j}, \quad (68b)$$

where $\mathbf{C}_{i,j}$ and $D_{i,j}$ are correction terms, which are linear combinations of jump values $[u]$, $[v]$, $[p]$, $[u_x]$, $[u_y]$, \dots . The resulting linear system (68) is solved with an efficient V-cycle geometric multigrid method with the Distributive Gauss-Seidel (DGS) smoother [59, 60].

Remark 4.1. Since particular solution parts have higher regularity, classical numerical approaches, such as finite difference methods, finite element methods, and spectral methods, can be applied. In this work, the particular parts are also solved with a five-point central difference scheme and the MAC scheme without any correction terms near the interface.

4.3. Extracting boundary values from the grid data

The single- and double-layer potential functions $S\psi$ and $D\varphi$ defined by boundary integrals are not smooth on Γ . Define the single- and double-layer boundary integral operators $\mathcal{L}\psi$ and $\mathcal{K}\varphi$ as values of the potential functions $S\psi$ and $D\varphi$ on Γ , respectively. By potential theory, for smooth Γ , the integral operators satisfy

$$\mathcal{L}\psi(\mathbf{x}) = \frac{1}{2}((S\psi)^+(\mathbf{x}) + (S\psi)^-(\mathbf{x})), \quad \mathbf{x} \in \Gamma, \quad (69)$$

$$\mathcal{K}\varphi(\mathbf{x}) = \frac{1}{2}((D\varphi)^+(\mathbf{x}) + (D\varphi)^-(\mathbf{x})), \quad \mathbf{x} \in \Gamma. \quad (70)$$

The normal derivatives of the potential functions $\partial_n(S\psi)$ and $\partial_n(D\varphi)$ have similar expressions

$$\partial_n(S\psi)(\mathbf{x}) = \mathbf{n}(\mathbf{x}) \cdot \frac{1}{2}((\nabla S\psi)^+(\mathbf{x}) + (\nabla S\psi)^-(\mathbf{x})), \quad \mathbf{x} \in \Gamma, \quad (71)$$

$$\partial_n(D\varphi)(\mathbf{x}) = \mathbf{n}(\mathbf{x}) \cdot \frac{1}{2}((\nabla D\varphi)^+(\mathbf{x}) + (\nabla D\varphi)^-(\mathbf{x})), \quad \mathbf{x} \in \Gamma. \quad (72)$$

The normal derivatives of potential functions are closely related to adjoint double-layer integral and hyper-singular integral operators [56]. As long as the grid-valued single- and double-layer potential functions $(S\psi)_h$ and $(D\varphi)_h$ are obtained, boundary integral operators can be computed by extracting boundary values and normal derivatives of the potential functions from grid data via polynomial interpolation

In doing the interpolation, one should take into account the jump values of the potential functions. Suppose one needs to evaluate the one-sided limit of a discontinuous function $v(\mathbf{x})$ at a point $\mathbf{p} = (p_1, p_2)^T \in \Gamma$ from the side of Ω^+ . Denote by $v^+(\mathbf{x})$ and $v^-(\mathbf{x})$ two functions that coincide with $v(\mathbf{x})$ in Ω^+ and Ω^- , respectively. Given a set of interpolation points $\{\mathbf{q}_m\}_{m=1}^M$, by Taylor expansion at \mathbf{p} , we have

$$v(\mathbf{q}_m) = v^+(\mathbf{p}) + (\Delta\mathbf{x}_m)^T \nabla v^+(\mathbf{p}) + \frac{1}{2}(\Delta\mathbf{x}_m)^T \nabla^2 v^+(\mathbf{p}) \Delta\mathbf{x}_m + \mathcal{O}(|\Delta\mathbf{x}_m|^3), \quad \text{if } \mathbf{q}_m \in \Omega^+, \quad (73)$$

$$v(\mathbf{q}_m) + C(\mathbf{q}_m) = v^+(\mathbf{p}) + (\Delta\mathbf{x}_m)^T \nabla v^+(\mathbf{p}) + \frac{1}{2}(\Delta\mathbf{x}_m)^T \nabla^2 v^+(\mathbf{p}) \Delta\mathbf{x}_m + \mathcal{O}(|\Delta\mathbf{x}_m|^3), \quad \text{if } \mathbf{q}_m \in \Omega^-, \quad (74)$$

where $\Delta \mathbf{x}_m = \mathbf{q}_m - \mathbf{p}$, $m = 1, \dots, M$ and $C(\mathbf{p})$ is given by

$$C(\mathbf{q}_m) = [v](\mathbf{p}) + (\Delta \mathbf{x}_m)^T [\nabla v](\mathbf{p}) + \frac{1}{2} (\Delta \mathbf{x}_m)^T [\nabla^2 v](\mathbf{p}) \Delta \mathbf{x}_m. \quad (75)$$

Dropping the $O(|\Delta \mathbf{x}_m|^3)$ term, one obtains an $M \times M$ linear system to be solved for the boundary values v^+ , ∇v^+ , $\nabla^2 v^+$. Then, the values v^- , ∇v^- , $\nabla^2 v^-$ can also be obtained after simple algebraic manipulations. To select interpolation points, for example, we first find the closest grid node (x_{i_0}, y_{j_0}) to \mathbf{p} . Let d_1, d_2 be two integers,

$$d_1 = \begin{cases} 1, & \text{if } p_1 > x_{i_0}, \\ -1, & \text{if } p_1 \leq x_{i_0}, \end{cases} \quad d_2 = \begin{cases} 1, & \text{if } p_2 > y_{j_0}, \\ -1, & \text{if } p_2 \leq y_{j_0}, \end{cases} \quad (76)$$

Then six interpolation points are chosen

$$\{(x_{i_0+r}, y_{j_0+s})\}_{(r,s) \in \mathcal{I}}, \quad \mathcal{I} = \{(0, 0), (1, 0), (0, 1), (0, -1), (-1, 0), (d_1, d_2)\}. \quad (77)$$

This choice of interpolation points results in a 6×6 system, which can be solved with a direct method, such as the LU decomposition.

5. Interface evolution method

5.1. The $\theta - L$ approach

Suppose the interface Γ is represented as a closed curve given by $\mathbf{X}(\alpha, t) = (x(\alpha, t), y(\alpha, t))$, where $\alpha \in [0, 2\pi)$ parameterizes the curve. The evolution of the curve is given by

$$\mathbf{X}_t = U \mathbf{n} + V \mathbf{s}, \quad (78)$$

where \mathbf{n} is the unit outward normal, \mathbf{s} is the unit tangent, U and V are the normal and tangential components of the curve velocity, respectively. In most cases, only the shape of the moving interface is of practical interest, which can be solely determined by the normal motion since the tangential motion only changes the parameterization. However, pure normal motion for tracking a moving interface is not a good choice for numerical computation due to the clustering or spread of marker points on the interface. Another issue is that the curvature term introduces numerical stiffness into the interface evolution and causes strict stability constraints on the time step. To mitigate these issues, we use the $\theta - L$ approach instead of (78) for the curve evolution,

$$L_t = \int_0^{2\pi} \theta_{\alpha'} U d\alpha', \quad (79)$$

$$\theta_t = \left(\frac{2\pi}{L}\right)(\theta_\alpha V - U_\alpha). \quad (80)$$

where θ is the tangent angle to the curve Γ and L is the curve length. By setting $s_\alpha = \sqrt{x_\alpha^2 + y_\alpha^2} \equiv L/2\pi$ for equal-arclength parameterization, one obtains the artificial tangential velocity

$$V(\alpha, t) = \frac{\alpha}{2\pi} \int_0^{2\pi} \theta_{\alpha'} U d\alpha' - \int_0^\alpha \theta_{\alpha'} U d\alpha', \quad (81)$$

The mapping from (θ, L) to $\mathbf{X} = (x, y)$ still needs two more integration constants to determine the position of the curve, for which we track $\bar{\mathbf{X}} = \frac{1}{2\pi} \int_0^{2\pi} \mathbf{X} d\alpha$ using the evolution equation

$$\bar{\mathbf{X}}_t = \frac{1}{2\pi} \int_0^{2\pi} U \mathbf{n} + V \mathbf{s} d\alpha. \quad (82)$$

While it is possible to track a single point, as demonstrated in [14], we find that using the averaged value provides better rotational symmetry.

5.2. Small scale decomposition

In the Hele-Shaw flow, the mapping from curvature κ to velocity U is a one-phase Dirichlet-to-Neumann (DtN) mapping [61], denoted as $\mathcal{T}_1 : \sigma\kappa \rightarrow U$. Upon small scale decomposition, it is found that the highest-order term in U , which contributes to the stiffness, is linear. Specifically, we have

$$U \sim -\frac{\sigma}{2} \left(\frac{2\pi}{L} \right)^2 \mathcal{H}[\theta_{\alpha\alpha}], \quad (83)$$

where \mathcal{H} represents the Hilbert transform [14]. This approach offers a straightforward means to develop efficient semi-implicit schemes for alleviating the stiffness associated with the curvature term.

For the Stefan problem, the mapping $\mathcal{T}_2 : \varepsilon_C \kappa \rightarrow U$ is a two-phase DtN mapping. We shall also derive a small-scale decomposition for the normal velocity U . For simplicity, we assume ε_V and ε_C are constants. Due to the relation $U = \psi$, the DtN mapping is defined through the boundary integral equation (32). Since the integral equation (32) becomes a Fredholm integral equation of the first kind if $\varepsilon_V = 0$, we need to consider two cases: (1) $\varepsilon_V = \mathcal{O}(1)$, and (2) $\varepsilon_V \ll 1$.

5.2.1. The first case: $\varepsilon_V = \mathcal{O}(1)$

Denote by $K\psi = (1/\varepsilon_V) \int_{\Gamma} G_c(\mathbf{y}, \mathbf{x}) \psi(\mathbf{y}) ds_{\mathbf{y}}$ and $g = -(\varepsilon_C/\varepsilon_V)\kappa - T_1/\varepsilon_V$. We write the boundary integral equation (32) as an operator equation

$$(I - K)\psi = g, \quad (84)$$

where the operator K is compact and $I - K$ has a bounded inverse. Then, we have

$$\psi = g + K\psi = g + K[(I - K)^{-1}g]. \quad (85)$$

The integral operator K is a pseudo-differential operator of order -1 and defines the mapping $K : C^\beta(\Gamma) \rightarrow C^{1+\beta}(\Gamma)$ for a fix constant β . Therefore, the term $S[(I - S)^{-1}g]$ is more regular than g . Further, since T_1 is equivalent to a volume integral, which is more regular than $\kappa = \theta_\alpha/s_\alpha = 2\pi\theta_\alpha/L$, we obtain

$$U \sim -\frac{\varepsilon_C}{\varepsilon_V} \left(\frac{2\pi}{L} \right) \theta_\alpha. \quad (86)$$

5.2.2. *The second case: $\varepsilon_V \ll 1$*

We rewrite ψ as a formal asymptotic expansion $\psi = \psi_0 + \varepsilon_V \psi_1 + \varepsilon_V^2 \psi_2 + \dots$ and substitute it into the boundary integral equation (32). The leading order equation implies that ψ_0 should satisfy

$$\int_{\Gamma} G_c(\mathbf{y}, \mathbf{x}) \psi_0(\mathbf{y}) d\mathbf{s}_y = \varepsilon_C \kappa(\mathbf{x}) + T_1(\mathbf{x}), \quad \text{for } \mathbf{x} \in \Gamma. \quad (87)$$

Since we only need the highest-order term in the small scale decomposition, we can simply proceed by assuming $\varepsilon_V = 0$ in (32) and use a similar technique as that in [30] to obtain the small scale decomposition. Note that the Green function $G_c(\mathbf{y}, \mathbf{x})$ associated with the modified Helmholtz operator $\Delta - c^2$ has the same singular behavior as the Green function $G_0(\mathbf{y}, \mathbf{x})$ associated with the Laplacian Δ . A simple singularity subtraction leads to

$$\frac{1}{2\pi} \int_{\Gamma} \ln |\mathbf{y} - \mathbf{x}| \psi(\mathbf{y}) d\mathbf{s}_y - \int_{\Gamma} (G_0(\mathbf{y}, \mathbf{x}) - G_c(\mathbf{y}, \mathbf{x})) \psi(\mathbf{y}) d\mathbf{s}_y = \varepsilon_C \kappa(\mathbf{x}) + T_1(\mathbf{x}), \quad \text{for } \mathbf{x} \in \Gamma, \quad (88)$$

where the kernel $G_0(\mathbf{y}, \mathbf{x}) - G_c(\mathbf{y}, \mathbf{x})$ no longer has a *log*-type singularity. Hence, in the left-hand side of (88), the second term is more regular than the first one. For every 2π -periodic function v , define the operators \mathcal{M} and \mathcal{R} by

$$\mathcal{M}[v](\alpha) = \frac{1}{2\pi} \int_0^{2\pi} \ln \left| 2 \sin \frac{\alpha - \alpha'}{2} \right| v(\alpha') d\alpha', \quad (89)$$

$$\mathcal{R}[v](\alpha) = \frac{1}{2\pi} \int_0^{2\pi} \ln \left| \frac{\mathbf{x}(\alpha) - \mathbf{x}(\alpha')}{2 \sin \frac{\alpha - \alpha'}{2}} \right| v(\alpha') d\alpha'. \quad (90)$$

Using the relation $s_\alpha \equiv L/2\pi$, the equation (88) can be written as

$$\frac{L}{2\pi} (\mathcal{M}[\psi] + \mathcal{R}[\psi]) - \int_{\Gamma} (G_0(\mathbf{y}, \mathbf{x}) - G_c(\mathbf{y}, \mathbf{x})) \psi(\mathbf{y}) d\mathbf{s}_y = \varepsilon_C \frac{2\pi}{L} \theta_\alpha + T_1. \quad (91)$$

Note that for every 2π -periodic function v , the relation $\mathcal{M}^{-1}[v] = c - 2\mathcal{H}[v]$ holds, where c is an arbitrary constant. Taking \mathcal{M}^{-1} on both sides of (91), it yields

$$\psi - \bar{\psi} = -2\varepsilon_C \left(\frac{2\pi}{L} \right)^2 \mathcal{H}[\theta_{\alpha\alpha}] - \frac{4\pi}{L} \mathcal{H} \left[\int_{\Gamma} (G_0(\mathbf{y}, \mathbf{x}) - G_c(\mathbf{y}, \mathbf{x})) \psi(\mathbf{y}) d\mathbf{s}_y + T_1 - \frac{L}{2\pi} \mathcal{R}[\psi] \right]_\alpha, \quad (92)$$

where $\bar{\psi}$ is the mean of ψ . Finally, since the second term in the right-hand side of (92) is more regular than the first term, we have

$$U \sim -2\varepsilon_C \left(\frac{2\pi}{L} \right)^2 \mathcal{H}[\theta_{\alpha\alpha}], \quad (93)$$

By inserting U into the θ evolution equation (80) and using the small scale expressions equations (86) and (93), we can extract the linear and highest-order terms

$$\theta_t = \begin{cases} \frac{\varepsilon_C}{\varepsilon_V} \left(\frac{2\pi}{L} \right)^2 \theta_{\alpha\alpha} + \mathcal{N}(\alpha), & \text{if } \varepsilon_V = \mathcal{O}(1), \\ 2\varepsilon_C \left(\frac{2\pi}{L} \right)^3 \mathcal{H}[\theta_{\alpha\alpha\alpha}] + \mathcal{N}(\alpha), & \text{if } \varepsilon_V \ll 1, \end{cases} \quad (94)$$

where \mathcal{N} consists of the remaining lower-order terms. The case $\varepsilon_V = \mathcal{O}(1)$ is second-order diffusive and is similar to a heat equation or a mean curvature flow. The stiffness of the second-order derivative term can be removed by employing an implicit time-stepping scheme for the stiff term. The second case $\varepsilon_V \ll 1$ is third-order diffusive [14]. Implicit schemes for the case are more difficult due to the nonlocal Hilbert transform \mathcal{H} . Using the fact that \mathcal{H} is diagonalizable under the Fourier transform, an accurate and efficient semi-implicit scheme can be devised.

5.3. Semi-implicit scheme

The evolution equations (79) and (82) are not stiff, they can be discretized with an explicit scheme. We use the second-order Adams-Bashforth scheme,

$$L^{n+1} = L^n + \tau(3M^n - M^{n-1}), \quad M = - \int_0^{2\pi} \theta_{\alpha'} U d\alpha', \quad (95)$$

$$\bar{\mathbf{X}}^{n+1} = \bar{\mathbf{X}}^n + \tau(3Q^n - Q^{n-1}), \quad Q = \frac{1}{2\pi} \int_0^{2\pi} V_n \mathbf{n} + V_s \mathbf{s} d\alpha. \quad (96)$$

The evolution equation (80) involves a stiff term, but it is hidden in the normal velocity U through a DtN mapping. In order to both remove the stiffness and avoid solving nonlinear algebraic systems, only the highest-order term in (80) is discretized implicitly. We first rewrite equation (80) as

$$\theta_t = \left(\frac{2\pi}{L}\right)(U_\alpha + \theta_\alpha T) + (\mathcal{L}(\alpha) - \mathcal{L}(\alpha)) = \mathcal{L}(\alpha) + \mathcal{N}(\alpha), \quad (97)$$

where \mathcal{L} is the highest-order and linear term and \mathcal{N} consists of the remaining lower-order terms. We have $\mathcal{L} = \mathcal{L}_1 = \lambda_1(2\pi/L)^2 \theta_{\alpha\alpha}$ for (86) and $\mathcal{L} = \mathcal{L}_2 = \lambda_2(2\pi/L)^3 \mathcal{H}[\theta_{\alpha\alpha\alpha}]$ for (83) and (93), where λ_1 and λ_2 are two constant parameters. For the Hele-Shaw flow and the Stefan problem with constant ε_C and ε_V , the parameters λ_1 and λ_2 can be chosen to match the corresponding constant factors in the highest-order terms. For the Stefan problem with anisotropic ε_C and ε_V , λ_1 and λ_2 are regarded as stabilization parameters, which should be chosen as sufficiently large to ensure stability. With a frozen coefficient analysis, we choose the parameters as

$$\lambda_1 = \max_{\alpha \in [0, 2\pi]} \left| \frac{\varepsilon_C(\mathbf{n}(\alpha))}{\varepsilon_V(\mathbf{n}(\alpha))} \right|, \quad \lambda_2 = \max_{\alpha \in [0, 2\pi]} [2\varepsilon_C(\mathbf{n}(\alpha))]. \quad (98)$$

In the Fourier space, the Hilbert transform \mathcal{H} becomes diagonal, and (97) simplifies to

$$\hat{\theta}_t(k) = -\lambda_1 \left(\frac{2\pi}{L}\right)^2 k^2 \hat{\theta}(k) + \hat{\mathcal{N}}(k) \quad \text{for } \mathcal{L} = \mathcal{L}_1, \quad (99)$$

$$\hat{\theta}_t(k) = -\lambda_2 \left(\frac{2\pi}{L}\right)^3 |k|^3 \hat{\theta}(k) + \hat{\mathcal{N}}(k) \quad \text{for } \mathcal{L} = \mathcal{L}_2. \quad (100)$$

A linear propagator and a second-order Adams-Bashforth method are used to discretize the stiff part and the non-stiff part in (99) and (100), respectively,

$$\hat{\theta}^{n+1}(k) = e_k(t_n, t_{n+1}) \hat{\theta}^n(k) + \frac{\tau}{2} (3e_k(t_n, t_{n+1}) \hat{\mathcal{N}}^n(k) - e_k(t_{n-1}, t_{n+1}) \hat{\mathcal{N}}^{n-1}(k)), \quad (101)$$

where the factors $e_k(t_n, t_{n+1})$ and $e_k(t_{n-1}, t_{n+1})$ are specified as

$$e_k(t_n, t_{n+1}) = \exp\left(-\frac{\lambda_1 \tau}{2} (2\pi k)^2 \left[\frac{1}{(L^n)^2} + \frac{1}{(L^{n+1})^2} \right]\right), \quad (102)$$

$$e_k(t_{n-1}, t_{n+1}) = \exp\left(-\lambda_1 \tau (2\pi k)^2 \left[\frac{1}{2(L^{n-1})^2} + \frac{1}{(L^n)^2} + \frac{1}{2(L^{n+1})^2} \right]\right), \quad (103)$$

for the case $\mathcal{L} = \mathcal{L}_1$ and

$$e_k(t_n, t_{n+1}) = \exp\left(-\frac{\lambda_2 \tau}{2} (2\pi |k|)^3 \left[\frac{1}{(L^n)^3} + \frac{1}{(L^{n+1})^3} \right]\right), \quad (104)$$

$$e_k(t_{n-1}, t_{n+1}) = \exp\left(-\lambda_2 \tau (2\pi |k|)^3 \left[\frac{1}{2(L^{n-1})^3} + \frac{1}{(L^n)^3} + \frac{1}{2(L^{n+1})^3} \right]\right). \quad (105)$$

for the case $\mathcal{L} = \mathcal{L}_2$.

Remark 5.1. The numerical operations for the evolution of θ and L , such as differentiation, integration, and solving ODEs, are all performed in the Fourier space using FFTs. This allows the interface evolution method to have spectral accuracy, resulting in smaller errors compared to second-order time integration methods. It is important to note that θ is periodic but has an increment of 2π from $\alpha = 0$ to $\alpha = 2\pi$. To obtain accurate results, one can use the auxiliary variable $\eta = \theta - \alpha$ when performing Fourier transforms.

6. Numerical results

In this section, we demonstrate the application of the proposed method in solving moving interface problems through numerical examples. In the first part, we focus on the Hele-Shaw flow. We examine the convergence of the method and utilize it to simulate the various dynamics of the Hele-Shaw bubble. By using the proposed method, we are able to accurately capture the complex behavior of the bubble, such as its growth and deformation. Furthermore, we showcase the method's ability to handle long-time computations by modeling a bubble that exhibits intricate finger-like structures. Moving on to the second part, we tackle the Stefan problem. We evaluate the convergence and stability of the method using multiple examples. The proposed method proves to be robust and accurate in solving the Stefan problem, allowing us to accurately track the solidification interface and capture its evolution over time. Additionally, we utilize the method to simulate dendritic solidification problems, both with and without the presence of flow effects in the liquid region. Through these examples, we demonstrate the versatility of the method in handling different scenarios and accurately capturing the complex dynamics of moving boundaries in solidification processes.

6.1. The Hele-Shaw flow

6.1.1. Convergence test

In this example, we investigate the convergence of the method for solving the Hele-Shaw flow. The initial shape we consider is a four-fold flower, defined as

$$(x(\alpha, 0), y(\alpha, 0)) = r(\alpha)(\cos \alpha, \sin \alpha), \quad r(\alpha) = 0.8 + 0.2 \cos 4\alpha, \quad \alpha \in [0, 2\pi). \quad (106)$$

The surface tension coefficient is chosen to be 0.01, and the numerical computation is performed within the bounding box of $[-1.5, 1.5]^2$. The air injection rate is set to zero, leading to the area-preserving property of the Hele-Shaw flow (since the fluid is incompressible). The numerical error is measured by comparing the enclosed area of the curve at $T = 1$ with the initial area. To study the spatial accuracy, we use a fixed time step size of $\tau = 1 \times 10^{-3}$ and vary the mesh size as $\Delta x = 3 \times 2^{-l}$, with $l = 5, 6, \dots, 9$. Similarly, to analyze the temporal accuracy, we use a fixed mesh size of $\Delta x = 3 \times 2^{-10}$ and vary the time step size as $\tau = 2^{-l} \times 10^{-3}$, with $l = 1, 2, \dots, 5$. We compute the enclosed area of the curve by numerically evaluating the integral $A[\Gamma] = \frac{1}{2} \int_{\Gamma} \mathbf{x} \cdot \mathbf{n} \, ds$. The numerical results are shown in Figure 2, and it can be observed that the method exhibits second-order accuracy both spatially and temporally.

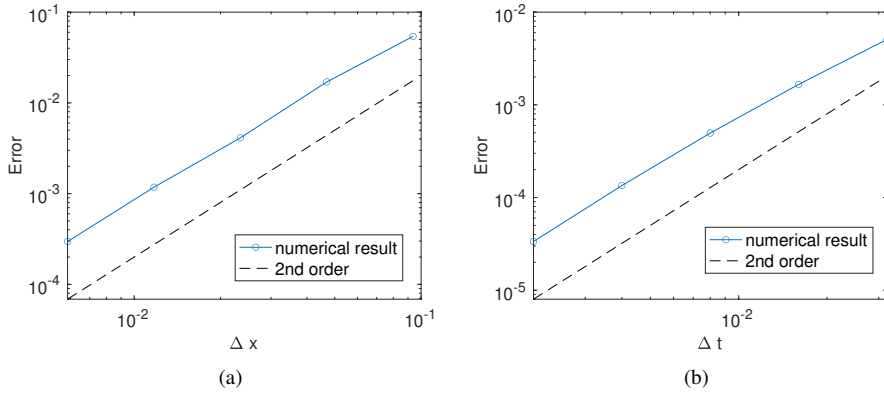


Figure 2: (a) shows the spatial accuracy of the method with different mesh sizes $\Delta x = 3 \times 2^{-l}$, $l = 5, 6, \dots, 9$. (b) shows the temporal accuracy of the method with different time steps $\tau = 2^{-l} \times 10^{-3}$, $l = 1, 2, \dots, 5$.

6.1.2. Bubble relaxation

The Hele-Shaw flow without air injection presents interesting characteristics due to the combined effects of surface tension and incompressibility. These effects result in a curve-shortening and area-preserving behavior [62]. In order to investigate this phenomenon, we consider an initial curve in the form of a six-fold flower, described by the parametric equation:

$$(x(\alpha, 0), y(\alpha, 0)) = r(\alpha)(\cos \alpha, \sin \alpha), \quad r(\alpha) = 0.8 + 0.2 \cos 6\alpha, \quad \alpha \in [0, 2\pi). \quad (107)$$

A surface tension coefficient of 0.01 is used, and the evolution is computed within a computational domain of $[-1.5, 1.5]^2$. The numerical simulation is conducted on a 512×512 grid, with a time step size of $\tau = 0.001$. The evolution of the curve is illustrated in Figure 3. Additionally, the area and length profiles of the curve, as well as the iteration numbers of the GMRES method, are presented in Figure 4. As a result of the stabilizing influence of surface tension, the initially irregular interface gradually relaxes and approaches a circular shape over time. Notably, the enclosed area remains constant throughout the evolution, while the length of the curve decreases over time and eventually converges. These observations align with the theoretical understanding of Hele-Shaw flow without air injection. The GMRES iteration number remains relatively stable and decreases as the curve approaches a circular shape.

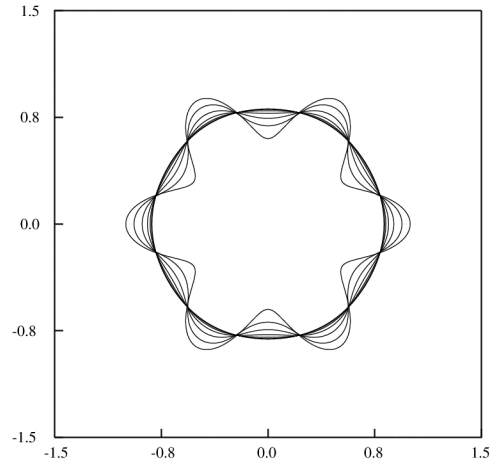


Figure 3: Morphologies of the interface from $t = 0$ to $t = 1.2$ with a time increment of 0.2.

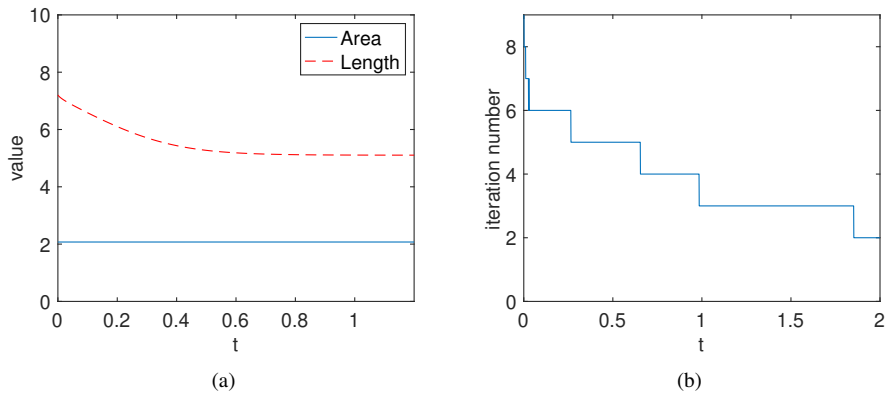


Figure 4: (a) shows the time evolutions of the enclosed area and the length of the curve. (b) shows the iteration number of the GMRES method.

6.1.3. Unstable viscous fingering

In this example, the initial curve is given by a three-fold flower,

$$(x(\alpha, 0), y(\alpha, 0)) = r(\alpha)(\cos \alpha, \sin \alpha), \quad r(\alpha) = 0.8 + 0.2 \cos 3\alpha, \quad \alpha \in [0, 2\pi). \quad (108)$$

The air injection rate is chosen as $J = 1$ such that the air bubble demonstrates an unstable growth. The surface tension coefficient varies from 1×10^{-2} to 5×10^{-4} . The computational domain is chosen as $[-4, 4]^2$. We solve the example on a 512×512 grid with a time step $\tau = 0.005$. The morphologies of the evolutionary curve are shown in Figure 5 in time increments of 0.2 to the final time $T = 3$. The competition between the stabilizing effect of the surface tension and the destabilizing effect of the driven force due to the injection leads to the viscous fingering feature of the Hele-Shaw flow. With small surface tension, which has a less stabilizing effect, the growing bubble develops more branches. It also can be observed that for small surface tensions, the symmetry of the interface is difficult to capture since grid-induced anisotropy dominates the interface evolution.

6.1.4. Long-time computation

In this example, we perform long-time computation with the present method and spatial-temporal rescaling scheme [15] for simulating a large Hele-Shaw bubble. The computation is performed in the scaled frame and then mapped back onto the nonscaled frame. The initial shape is chosen as a nucleus

$$(\bar{x}(\alpha, 0), \bar{y}(\alpha, 0)) = \bar{r}(\alpha)(\cos \alpha, \sin \alpha), \quad \bar{r}(\alpha) = 1.0 + 0.1(\sin 2\alpha + \cos 3\alpha), \quad \alpha \in [0, 2\pi). \quad (109)$$

The computational domain is chosen as $[-1.7, 1.7]^2$. We use a 1024×1024 grid and a time step of $\Delta \bar{t} = 2 \times 10^{-4}$. The interface points are adaptively refined with the criteria $\Delta \bar{s} > 1.5\Delta \bar{x}$. The injection rate and the surface tension coefficient are set as $\bar{J} = 1$ and $\sigma = 0.001$, respectively. The morphologies of the curve in the nonscaled frame are shown in (scaled) time increments of 0.2, in Figure 6. The computation takes 5 hours to reach the final scaled time $\bar{T} = 3$ (nonscaled time $T = 203$). At the final time, the number of the marker point on the interface is refined to 16384, and the enclosed area and the length of the interface are $A = \bar{R}^2 \bar{A} = 1280$ and $L = \bar{R} \bar{L} / 2\pi = 169$.

6.2. The Stefan problem

6.2.1. Grid refinement analysis

In this example, we consider a benchmark grid refinement test for the Stefan problem. In the beginning, a solid seed is put into an undercooling liquid domain $\mathcal{B} = [-2, 2]^2$. The initial shape is a four-fold flower, which is given by

$$(x(\alpha, 0), y(\alpha, 0)) = r(\alpha)(\cos \alpha, \sin \alpha), \quad r(\alpha) = 0.1 + 0.02 \cos 4\alpha, \quad \alpha \in [0, 2\pi). \quad (110)$$

The initial undercooling is chosen as $St = -0.5$. Isotropic surface tension and kinematic coefficients are chosen as $\varepsilon_C = \varepsilon_V = 2 \times 10^{-3}$. We take the time step as $\tau = 0.001$ and successively refine the grid from 64 to 512. The morphologies of the liquid-solid interface in time increments of 0.05 to the final time $T = 0.8$ are shown in Figure 7. By comparing the results with previous works by the level-set method and the front-tracking method [16, 20], it can be observed that our method has less grid-induced surface tension, which leads to better convergence. The method is also more able to preserve the symmetries of the interface, even with a coarse grid.

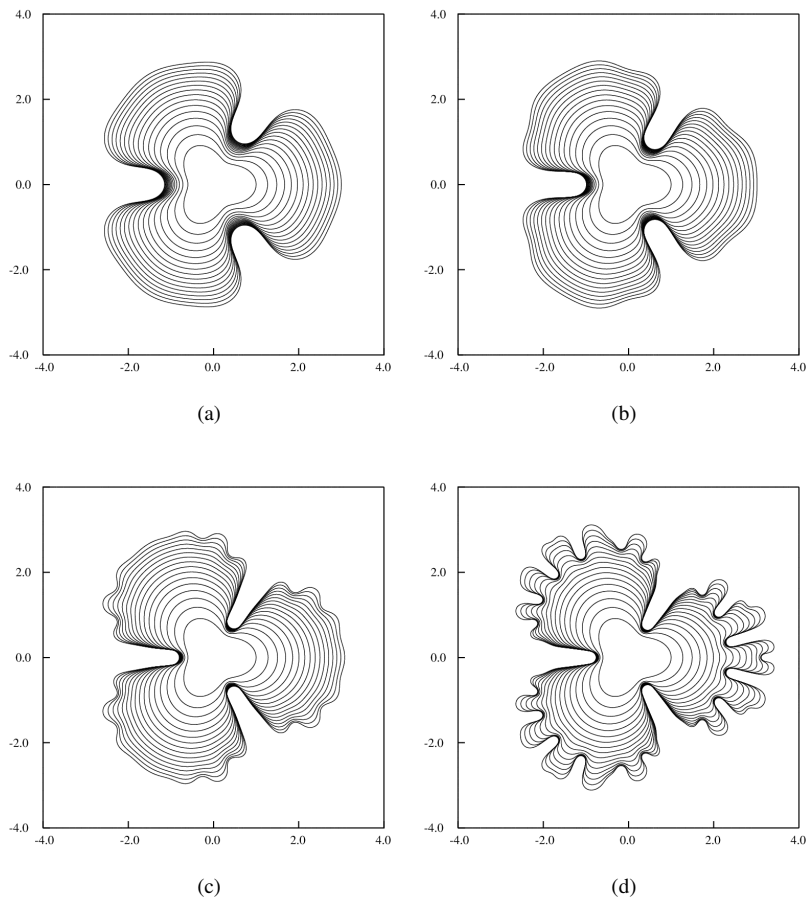
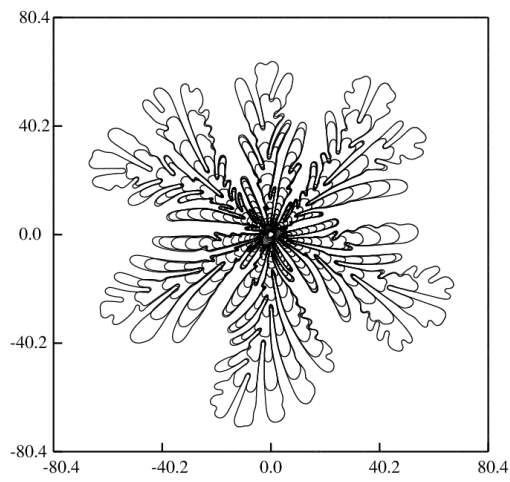
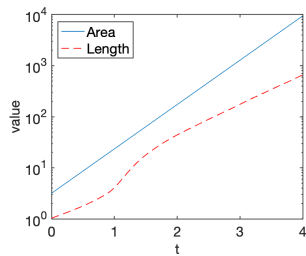


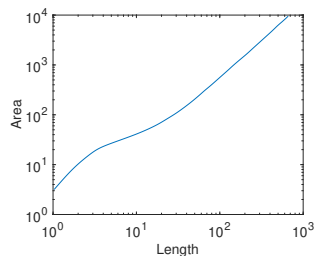
Figure 5: Detailed morphologies of the curve with different surface tension coefficients: (a) 1×10^{-2} ; (b) 5×10^{-3} ; (c) 1×10^{-3} ; (d) 5×10^{-4} .



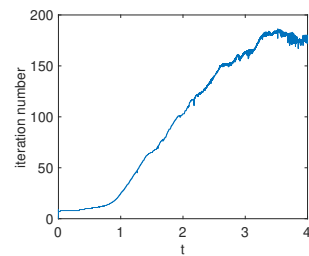
(a)



(b)



(c)



(d)

Figure 6: Numerical results of long-time computation of the Hele-Shaw flow: (a) morphology histories of the curve; (b) and (c) time evolution of the curve length and enclosed area; (d) iteration numbers of the GMRES method.

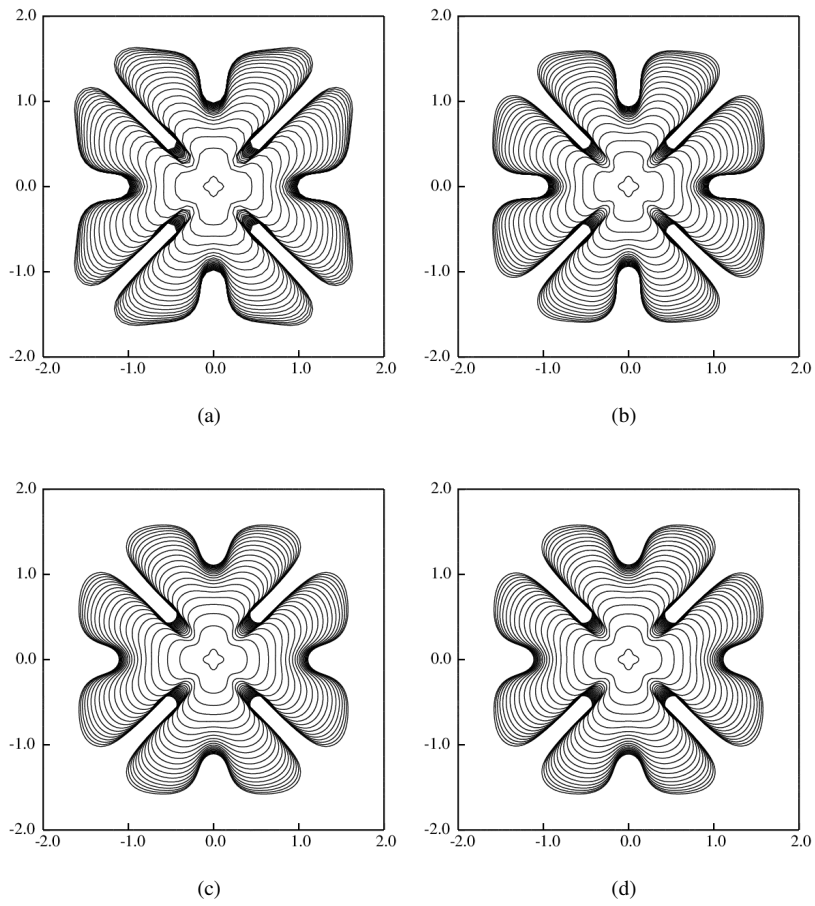


Figure 7: Grid refinement analysis of the Stefan problem with different grids: (a) 64×64 ; (b) 128×128 ; (c) 256×256 ; (d) 512×512 .

6.2.2. Stability test

In order to demonstrate the stability of the method, we compare the semi-implicit scheme with an explicit Adams-Bashforth scheme. We consider the case that $\varepsilon_V = 0$ and $\varepsilon_C = 0.05$, which results in a third-order stiffness. The initial shape is chosen as a slightly perturbed circle

$$(x(\alpha, 0), y(\alpha, 0)) = r(\alpha)(\cos \alpha, \sin \alpha), \quad r(\alpha) = 1 + 0.02 \cos 4\alpha, \quad \alpha \in [0, 2\pi). \quad (111)$$

We use a 256×256 grid for the computational domain $\mathcal{B} = [-2, 2]^2$. The interface is discretized with 128 points. First, the problem is solved with an explicit scheme with time-steps $\tau = 5 \times 10^{-5}$ and $\tau = 2.5 \times 10^{-5}$. The curves at $t = 0.1$ are plotted in Figure 8(a). The smaller time-step $\tau = 2.5 \times 10^{-5}$ is stable for the computation, while the larger one $\tau = 5 \times 10^{-5}$ is unstable, and the solution quickly blows up. Then, the problem is solved with the semi-implicit scheme with a time-step $\tau = 0.01$, and the solution at $t = 0$ is plotted in Figure 8(b). Compared with the explicit scheme, the semi-implicit scheme is stable and can obtain a correct result with a much larger time step, which makes the semi-implicit scheme more efficient.

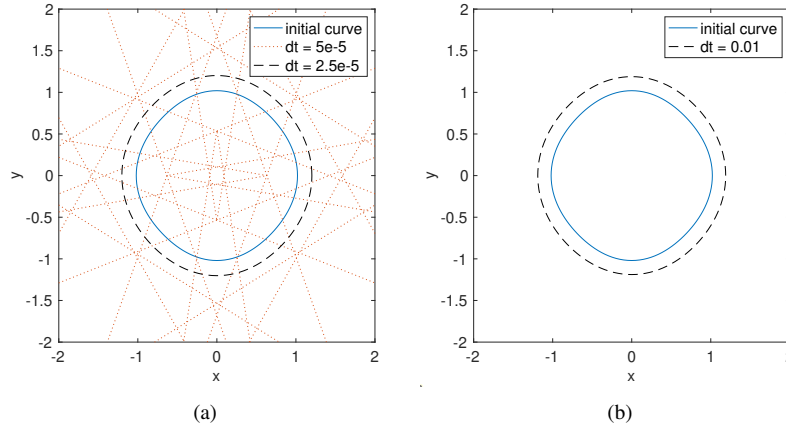


Figure 8: Numerical results of the stability test for the Stefan problem with different time-stepping methods: (a) the Adams-Bashforth scheme; (b) the semi-implicit scheme.

6.2.3. Comparison with the solvability theory

In a dendritic growth problem, the growth rate of a dendrite can be predicted by the solvability theory [9, 63]. We compare the numerical result with the solvability result to assess the accuracy of the method. In this example, the initial seed is chosen as a circle with a radius of 0.1. The parameters in the Gibbs-Thomson relation are chosen as $\varepsilon_V = 0$, $\varepsilon_C(\alpha) = 0.001[1 + 0.4(1 - \cos(4\alpha))]$ where α is the angle between the normal to the interface and the x -axis. The computation domain is chosen as $[-6, 6]$. We set $\tau = 0.001$ for the computation. The morphologies of the liquid-solid interface and the time-evolution of the tip velocity from $t = 0$ to $t = 2.2$ are plotted in Figure 9. The tip velocity finally converges and agrees with the solvability result of 1.7.

6.2.4. Anisotropic dendritic growth

initial seed is a circle with a radius 0.05 at the center of the computational domain $[-4, 4]^2$. undercooling $S_t = -0.65$ four-fold anisotropy $\varepsilon_V = 0.002$, $\varepsilon_C(\alpha) = 0.002(8/3 \sin^4(2(\alpha - \alpha_0)))$

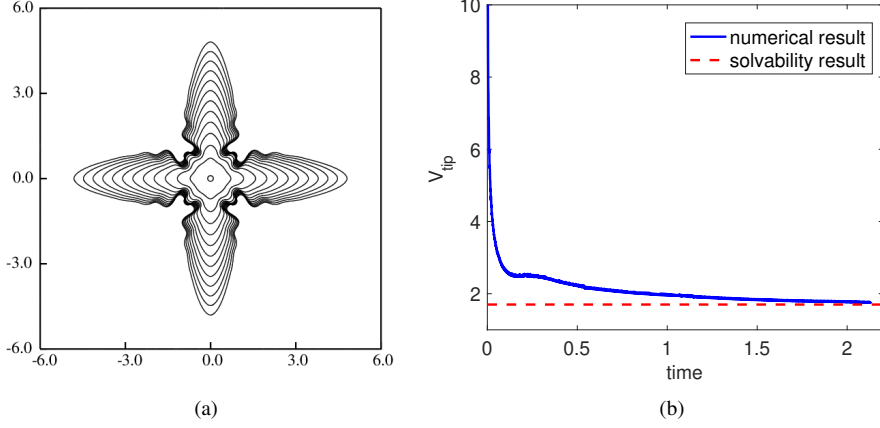


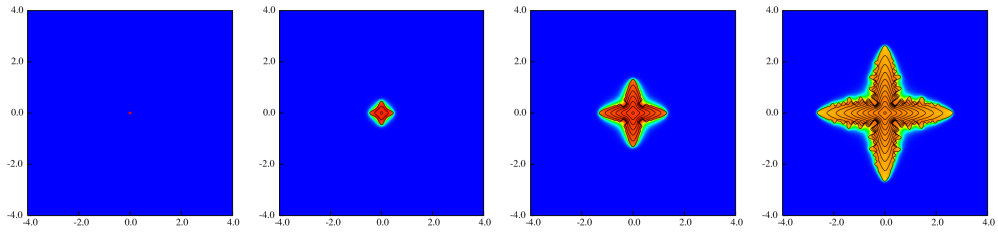
Figure 9: Numerical results of the dendritic growth problem and comparison with the solvability theory: (a) morphology histories of the interface; (b) time evolution of the tip velocity.

grid 512×512 with a time step $\tau = 0.0002$.

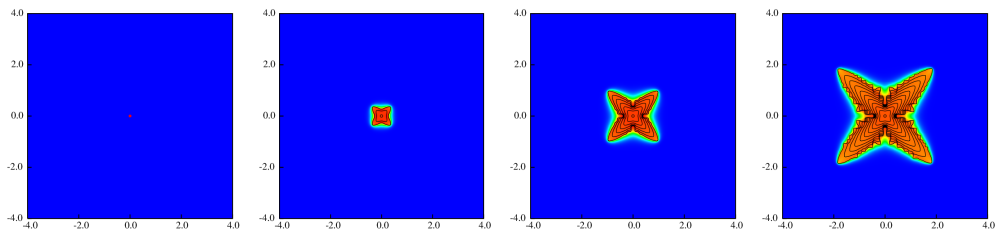
The initial seed is a circle with a radius 0.05 at the center of the computational domain $\mathcal{B} = [-2, 2]^2$. The undercooling parameter varies from $St = -0.55$ to $St = -0.65$. The parameters in the Gibbs-Thomson relation are chosen as $\varepsilon_V = 0.002$, $\varepsilon_C(\alpha) = 0.002(8/3 \sin^4(3\alpha))$, which is a six-fold anisotropy. The six-fold anisotropy leads to snowflake-shaped dendritic growths, which are shown in Figure 11.

6.2.5. Dendritic growth with external flow

We consider the convection effect in the dendritic growth problem. In this example, the Stefan problem with natural convection is solved for simulations. Initially, the seed is a circle with a radius 0.05 at the center of the computational domain $[-2, 2]^2$ surrounded by undercooled fluid with temperature $St = -0.5$. Four-fold anisotropic surface tension $\varepsilon_C(\alpha) = 0.002(8/3 \sin^4(2\alpha))$ and local kinematic equilibrium $\varepsilon_V = 0$ are applied. The computation is performed with a 512×512 grid and a time step $\tau = 0.0002$. Inflow and outflow boundary conditions, $\mathbf{u} = (u_0, 0)^T$, are applied on the left and right boundaries, respectively. No-slip boundary condition, $\mathbf{u} = \mathbf{0}$, is used on the top and bottom boundaries. In this example, we ignore the buoyancy force, i.e. $\beta = 0$. As a result, the convection of the flow is only driven by boundary conditions. When $u_0 = 0$, the problem is identical to the classical Stefan problem without natural convection. In order to examine the convection effect on the growth pattern, we compare numerical results obtained with different flow velocities in the fluid phase. In Figure 12, profiles of dendritic growth, temperature, and flow fields at $t = 0.1$ are presented. Evolution histories of x -components of the left and right tips are shown in Figure 13. It can be observed that convection of the flow leads to faster growth of the left branch and slower growth of the right branch. This effect is more evident as the flow velocity increases. Due to the flow convection, the released latent heat is carried by the flow from left to right and consequently leads to non-symmetric temperature distribution in the x -direction.

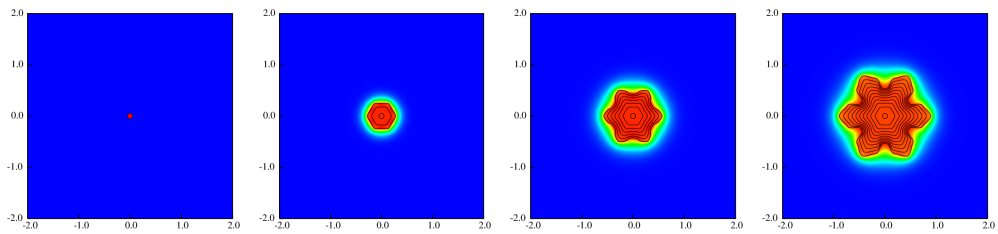


(a) Numerical results with $\alpha_0 = 0$.

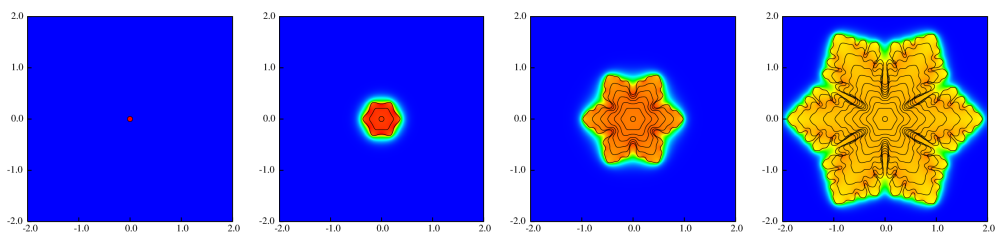


(b) Numerical results with $\alpha_0 = \pi/4$.

Figure 10: Interface morphologies and the temperature field of the dendritic growth problem with four-fold anisotropy. Snapshots are taken at $t = 0, 0.02, 0.06$, and 0.1 .



(a) Numerical results with $S t = -0.55$.



(b) Numerical results with $S t = -0.65$.

Figure 11: Interface morphologies and the temperature field of the dendritic growth problem with six-fold anisotropy. Snapshots are taken at $t = 0, 0.02, 0.06$, and 0.1 .

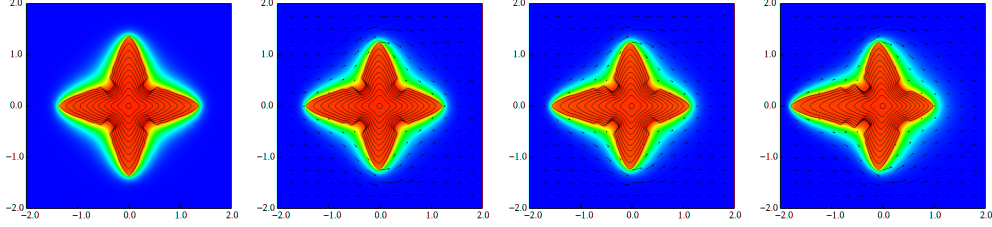


Figure 12: Details of dendritic growth histories, temperature fields, and flow fields with different inflow velocities at $t = 0.1$ ($u_0 = 0, 2, 4$ and 8 from left to right).

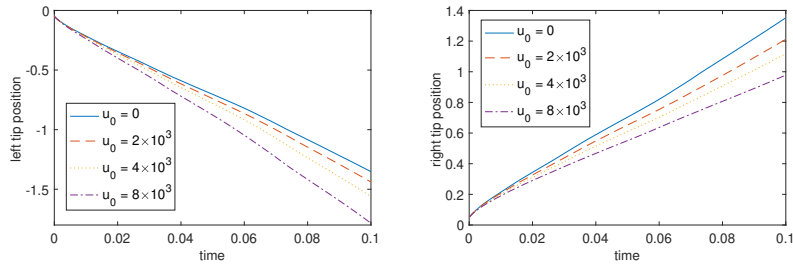


Figure 13: Evolution histories of x -components of the left and right tips with different flow velocities.

6.2.6. Dendritic growth with buoyancy-driven flow

In the final example, we consider the dendritic growth problem with buoyancy-driven flow. The anisotropic surface tension is chosen as a rotated one, $\varepsilon_C(\alpha) = 0.002(8/3 \sin^4(2(\alpha - \pi/4)))$. The no-slip boundary condition is applied for the fluid equation on the four boundaries. Different thermal expansion coefficients are chosen so that the flow in the fluid phase is driven by buoyancy force. The gravity acceleration is chosen as $g = 10$. The reference temperature is chosen as the temperature of surrounding fluid $T_0 = -0.5$. Other parameters are chosen as the same as those in the last example. Numerical results with increasing thermal expansion coefficients are presented in Figure 14. Near the solid-liquid interface, the released latent heat increases the fluid temperature and, as a result, causes fluid density changes and the buoyancy force. Driven by the buoyancy force, the fluid carries the heat and flows from bottom to top, which leads to non-symmetric temperature distribution in y -direction. The two upper branches are restrained from growing due to accumulated heat, while the two lower branches grow much faster since the heat flows away.

7. Discussion

This study presents a novel numerical method for solving two representative moving interface problems using a Cartesian grid-based boundary integral method combined with an interface evolution approach. The proposed method offers several advantages that combine the strengths of Cartesian grid-based solvers and boundary integral methods.

Elliptic and parabolic PDEs with irregular boundaries or interfaces are reformulated as well-conditioned boundary integral equations and are solved using the KFBI method. The KFBI

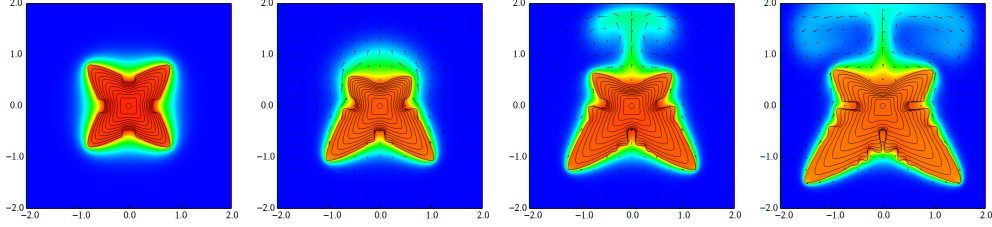


Figure 14: Details of dendritic growth histories, temperature fields, and flow fields with different thermal expansion coefficients at $t = 0.1$ ($\beta = 0, 10^3, 2 \times 10^3$ and 4×10^3 from left to right).

method utilizes a Cartesian grid-based solver for integral evaluations, eliminating the need for analytical expressions of Green's functions and allowing for efficient utilization of fast PDE solvers like FFTs and geometric multigrid methods. It is important to note that the method is not entirely kernel-free in this work. Green's function is still required to impose artificial boundary conditions on the rectangular domain boundary when dealing with infinite boundary conditions. However, the KFBI method avoids the evaluation of singular and nearly singular integrals, which are typically challenging in quadrature-based boundary integral methods.

The interface evolution is solved using the $\theta - L$ formulation instead of the more commonly used $x-y$ formulation. Due to the periodicity of the interface, an accurate Fourier pseudo-spectral method is employed for spatial approximation in the interface evolution problem. Furthermore, the use of the $\theta - L$ formulation enables the application of a small-scale decomposition approach to address the curvature-induced stiffness in the Hele-Shaw flow and Stefan problem. This approach, combined with a semi-implicit scheme, allows for efficient and stable evolution of the interface by solving the semi-implicit scheme in the Fourier space with the FFT.

While the current work primarily focuses on moving interface problems in two dimensions, certain improvements are needed to solve models in three dimensions, such as solidification problems and two-phase incompressible flows. First, elliptic PDEs with irregular boundaries and interfaces in three dimensions require a three-dimensional version of the KFBI method [52]. Additionally, for parabolic PDEs, dimension-splitting techniques can be employed to accelerate computation [64]. Second, the $\theta - L$ approach is only applicable to evolutionary curves in two dimensions. To accurately track evolutionary surfaces in three dimensions, different numerical approaches, such as the front-tracking method or the level-set method, are needed. Finally, addressing the stiffness induced by mean curvature in three dimensions poses greater challenges than in two dimensions. Developing an efficient semi-implicit time-stepping scheme is crucial for ensuring the stable evolution of the interface.

Appendix A. Computation of derivative jumps

Suppose Γ is parameterized as $\mathbf{X}(\alpha) = (x(\alpha), y(\alpha))$ where α is an arbitrary parameter. Let s be the arc-length parameter. Suppose Γ is sufficiently smooth, at least in the class C^2 . The unit outward normal is given by $\mathbf{n} = (y_\alpha/s_\alpha, -x_\alpha/s_\alpha)$ where $s_\alpha = \sqrt{x_\alpha^2 + y_\alpha^2}$. Given an interface problem with a constant coefficient, we shall derive jump values of the solution and its derivatives at the point $(x(\alpha), y(\alpha)) \in \Gamma$.

Appendix A.1. The modified Helmholtz equation

Consider the interface problem of the modified Helmholtz equation

$$\Delta u - c^2 u = f, \quad \text{in } \Omega^+ \cup \Omega^-, \quad (\text{A.1})$$

$$[u] = \Phi, \quad \text{on } \Gamma, \quad (\text{A.2})$$

$$[\partial_{\mathbf{n}} u] = \Psi, \quad \text{on } \Gamma. \quad (\text{A.3})$$

The interface condition (A.2) implies the zeroth-order jump value

$$[u] = \Phi. \quad (\text{A.4})$$

By taking the derivative of both sides of the interface condition (A.2) with respect to α and combining the interface condition (A.3), we have a 2×2 linear system

$$x_\alpha [u_x] + y_\alpha [u_y] = \Phi_\alpha, \quad (\text{A.5})$$

$$y_\alpha [u_x] - x_\alpha [u_y] = s_\alpha \Psi. \quad (\text{A.6})$$

Solving the linear system gives the values of $[u_x]$ and $[u_y]$. By taking the derivative of both sides of equations (A.5) and (A.6), and using equation (A.1), we have a 3×3 linear system for $[u_{xx}]$, $[u_{yy}]$ and $[u_{xy}]$

$$(x_\alpha)^2 [u_{xx}] + (y_\alpha)^2 [u_{yy}] + 2x_\alpha y_\alpha [u_{xy}] = \Phi_{\alpha\alpha} - x_{\alpha\alpha} [u_x] - y_{\alpha\alpha} [u_y], \quad (\text{A.7})$$

$$\begin{aligned} & x_\alpha y_\alpha [u_{xx}] - x_\alpha y_\alpha [u_{yy}] + ((y_\alpha)^2 - (x_\alpha)^2) [u_{xy}] \\ & = s_{\alpha\alpha} \Psi + s_\alpha \Psi_\alpha - y_{\alpha\alpha} [u_x] + x_{\alpha\alpha} [u_y], \end{aligned} \quad (\text{A.8})$$

$$[u_{xx}] + [u_{yy}] = c^2 \Phi + [f]. \quad (\text{A.9})$$

After solving the linear system, the derivative jump values are obtained.

Appendix A.2. The modified Stokes equation

Consider the interface problem of the modified Stokes equation

$$\Delta \mathbf{u} - c^2 \mathbf{u} - \nabla p = \mathbf{f}, \quad \text{in } \Omega^+ \cup \Omega^-, \quad (\text{A.10})$$

$$\nabla \cdot \mathbf{u} = 0, \quad \text{in } \Omega^+ \cup \Omega^-, \quad (\text{A.11})$$

$$[\mathbf{u}] = \Phi, \quad \text{on } \Gamma, \quad (\text{A.12})$$

$$[T(\mathbf{u}, p)] = \Psi, \quad \text{on } \Gamma. \quad (\text{A.13})$$

where $\mathbf{u} = (u, v)^T$, $T(\mathbf{u}, p) = -p\mathbf{n} + (\nabla \mathbf{u} + \nabla \mathbf{u}^T)\mathbf{n}$, $\mathbf{f} = (f_1, f_2)^T$, $\Phi = (\Phi_1, \Phi_2)^T$, $\Psi = (\Psi_1, \Psi_2)^T$. The zeroth-order jump values are obtained from equation (A.12),

$$[u] = \Phi_1, \quad [v] = \Phi_2. \quad (\text{A.14})$$

Taking the derivative of both sides of the interface condition (A.12) with respect to α and using equations (A.11) and (A.13), we obtain a 5×5 system for the first-order jump values $[u_x]$, $[u_y]$, $[v_x]$, $[v_y]$ and $[p]$,

$$x_\alpha [u_x] + y_\alpha [u_y] = \Phi_{1,\alpha}, \quad (\text{A.15})$$

$$x_\alpha [v_x] + y_\alpha [v_y] = \Phi_{2,\alpha}, \quad (\text{A.16})$$

$$2y_\alpha [u_x] - x_\alpha [u_y] - x_\alpha [v_x] - y_\alpha [p] = s_\alpha \Psi_1, \quad (\text{A.17})$$

$$y_\alpha [u_y] + y_\alpha [v_x] - 2x_\alpha [v_y] + x_\alpha [p] = s_\alpha \Psi_2, \quad (\text{A.18})$$

$$[u_x] + [v_y] = 0. \quad (\text{A.19})$$

Taking the derivative of both sides of equations (A.15) to (A.18) with respect to α and the derivatives of both sides of equation (A.11) with respect to x and y , and using equation (A.10), we obtain an 8×8 system for the second-order jump values $[u_{xx}]$, $[u_{yy}]$, $[u_{xy}]$, $[v_{xx}]$, $[v_{yy}]$, $[v_{xy}]$, $[p_x]$ and $[p_y]$,

$$(x_\alpha)^2[u_{xx}] + (y_\alpha)^2[u_{yy}] + 2x_\alpha y_\alpha[u_{xy}] = r_1, \quad (\text{A.20})$$

$$(x_\alpha)^2[v_{xx}] + (y_\alpha)^2[v_{yy}] + 2x_\alpha y_\alpha[v_{xy}] = r_2, \quad (\text{A.21})$$

$$2x_\alpha y_\alpha[u_{xx}] - x_\alpha y_\alpha[u_{yy}] + (2(y_\alpha)^2 - (x_\alpha)^2)[u_{xy}] - (x_\alpha)^2[v_{xx}] - x_\alpha y_\alpha[v_{xy}] - x_\alpha y_\alpha[p_x] - (y_\alpha)^2[p_y] = r_3, \quad (\text{A.22})$$

$$(y_\alpha)^2[u_{yy}] + x_\alpha y_\alpha[u_{xy}] + x_\alpha y_\alpha[v_{xx}] - 2x_\alpha y_\alpha[v_{yy}] + ((y_\alpha)^2 - 2(x_\alpha)^2)[v_{xy}] + (x_\alpha)^2[p_x] + x_\alpha y_\alpha[p_y] = r_4, \quad (\text{A.23})$$

$$[u_{xx}] + [u_{yy}] - [p_x] = c^2\Phi_1 + [f_1], \quad (\text{A.24})$$

$$[v_{xx}] + [v_{yy}] - [p_y] = c^2\Phi_2 + [f_2], \quad (\text{A.25})$$

$$[u_{xx}] + [v_{xy}] = 0, \quad (\text{A.26})$$

$$[u_{xy}] + [v_{yy}] = 0. \quad (\text{A.27})$$

where $r_i, i = 1, 2, \dots, 4$ are given by

$$r_1 = \Phi_{1,\alpha\alpha} - x_{\alpha\alpha}[u_x] - y_{\alpha\alpha}[u_y], \quad (\text{A.28})$$

$$r_2 = \Phi_{2,\alpha\alpha} - x_{\alpha\alpha}[v_x] - y_{\alpha\alpha}[v_y], \quad (\text{A.29})$$

$$r_3 = s_{\alpha\alpha}\Psi_1 + s_\alpha\Psi_{1,\alpha} - 2y_{\alpha\alpha}[u_x] + x_{\alpha\alpha}[u_y] + x_{\alpha\alpha}[v_x] + y_{\alpha\alpha}[p], \quad (\text{A.30})$$

$$r_4 = s_{\alpha\alpha}\Psi_2 + s_\alpha\Psi_{2,\alpha} - y_{\alpha\alpha}[u_y] - y_{\alpha\alpha}[v_x] + 2x_{\alpha\alpha}[v_y] - x_{\alpha\alpha}[p]. \quad (\text{A.31})$$

By solving the three linear systems, the derivative jump values of u, v, p can be obtained.

References

- [1] H.-D. Cao, B.-L. Chen, X.-P. Zhu, Recent developments on the Hamilton's Ricci Flow, *Surveys in Differential Geometry* 12 (1) (2007) 47–112. doi:10.4310/sdg.2007.v12.n1.a3.
- [2] X. Chen, Generation and propagation of interfaces for reaction-diffusion equations, *Journal of Differential Equations* 96 (1) (1992) 116–141. doi:10.1016/0022-0396(92)90146-E. URL <https://linkinghub.elsevier.com/retrieve/pii/002203969290146E>
- [3] G. BELLETTINI, M. PAOLINI, Anisotropic motion by mean curvature in the context of Finsler geometry, *Hokkaido Mathematical Journal* 25 (3) (1996) 537–566. doi:10.14492/hokmj/1351516749. URL <https://projecteuclid.org/journals/hokkaido-mathematical-journal/volume-25/issue-3/Anisotropic-motion-by-mean-curvature-in-the-context-of-Finsler/10.14492/hokmj/1351516749.full>
- [4] J. M. Hyman, Numerical methods for tracking interfaces, *Physica D: Nonlinear Phenomena* 12 (1) (1984) 396–407. doi:[https://doi.org/10.1016/0167-2789\(84\)90544-X](https://doi.org/10.1016/0167-2789(84)90544-X). URL <https://www.sciencedirect.com/science/article/pii/016727898490544X>
- [5] J. Glimm, D. Marchesin, O. McBryan, Statistical fluid dynamics: Unstable fingers, *Communications in Mathematical Physics* 74 (1) (1980) 1–13. doi:10.1007/BF01197574. URL <http://link.springer.com/10.1007/BF01197574>
- [6] J. Glimm, D. Marchesin, O. McBryan, Subgrid resolution of fluid discontinuities, II, *Journal of Computational Physics* 37 (3) (1980) 336–354. doi:10.1016/0021-9991(80)90041-8. URL <https://linkinghub.elsevier.com/retrieve/pii/0021999180900418>
- [7] W. W. Mullins, Two-dimensional motion of idealized grain boundaries, *Journal of Applied Physics* 27 (8) (1956) 900–904. doi:10.1063/1.1722511. URL <http://aip.scitation.org/doi/10.1063/1.1722511>

- [8] J. A. Sethian, J. Strain, Crystal growth and dendritic solidification, *Journal of Computational Physics* 98 (2) (1992) 231–253. doi:10.1016/0021-9991(92)90140-T.
- [9] D. I. Meiron, Selection of steady states in the two-dimensional symmetric model of dendritic growth, *Tech. Rep.* 4 (1986). doi:10.1103/PhysRevA.33.2704.
- [10] W. W. Mullins, R. F. Sekerka, Morphological Stability of a Particle Growing by Diffusion or Heat Flow, *Journal of Applied Physics* 34 (2) (1963) 323–329. doi:10.1063/1.1702607.
URL <https://pubs.aip.org/aip/jap/article/34/2/323-329/163811>
- [11] Y. Li, D. Jeong, J.-i. Choi, S. Lee, J. Kim, Fast local image inpainting based on the Allen–Cahn model, *Digital Signal Processing* 37 (1) (2015) 65–74. doi:10.1016/j.dsp.2014.11.006.
URL <http://dx.doi.org/10.1016/j.dsp.2014.11.006><https://linkinghub.elsevier.com/retrieve/pii/S1051200414003418>
- [12] M. Beneš, V. Chalupecký, K. Mikula, Geometrical image segmentation by the Allen-Cahn equation, *Applied Numerical Mathematics* 51 (2-3) (2004) 187–205. doi:10.1016/j.apnum.2004.05.001.
- [13] A. DEGREGORIA, L. SCHWARTZ, A boundary-integral method for two-phase displacement in hele-shaw cells, *Dynamics of Curved Fronts* (1988) 201–218doi:10.1016/B978-0-08-092523-3.50022-8.
- [14] T. Y. Hou, J. S. Lowengrub, M. J. Shelley, Removing the stiffness from interfacial flows with surface tension, *Journal of Computational Physics* 114 (2) (1994) 312–338. doi:10.1006/jcph.1994.1170.
- [15] S. Li, J. S. Lowengrub, P. H. Leo, A rescaling scheme with application to the long-time simulation of viscous fingering in a Hele-Shaw cell, *Journal of Computational Physics* 225 (1) (2007) 554–567. doi:10.1016/j.jcp.2006.12.023.
- [16] D. Juric, G. Tryggvason, A front-tracking method for dendritic solidification, *Journal of Computational Physics* 123 (1) (1996) 127–148. doi:10.1006/jcph.1996.0011.
- [17] J. Strain, A boundary integral approach to unstable solidification, *Journal of Computational Physics* 85 (2) (1989) 342–389. doi:10.1016/0021-9991(89)90155-1.
URL <https://www.sciencedirect.com/science/article/pii/0021999189901551><https://linkinghub.elsevier.com/retrieve/pii/0021999189901551>
- [18] P. Zhao, J. C. Heinrich, D. R. Poirier, Fixed mesh front-tracking methodology for finite element simulations, *International Journal for Numerical Methods in Engineering* 61 (6) (2004) 928–948. doi:<https://doi.org/10.1002/nme.1098>.
URL <https://onlinelibrary.wiley.com/doi/abs/10.1002/nme.1098>
- [19] A. Schmidt, Computation of Three Dimensional Dendrites with Finite Elements, *Journal of Computational Physics* 125 (2) (1996) 293–312. doi:10.1006/jcph.1996.0095.
URL <https://linkinghub.elsevier.com/retrieve/pii/S0021999196900959>
- [20] S. Chen, B. Merriman, S. Osher, P. Smereka, A simple level set method for solving stefan problems, *Tech. Rep.* 1 (1997). doi:10.1006/jcph.1997.5721.
- [21] Y.-T. Kim, N. Goldenfeld, J. Dantzig, Computation of dendritic microstructures using a level set method, *Physical Review E* 62 (2) (2000) 2471–2474. doi:10.1103/PhysRevE.62.2471.
URL <https://link.aps.org/doi/10.1103/PhysRevE.62.2471>
- [22] F. Gibou, R. Fedkiw, R. Caflisch, S. Osher, A Level Set Approach for the Numerical Simulation of Dendritic Growth, *Tech. Rep.* 1-3 (2003). doi:10.1023/A:1025399807998.
- [23] L. Boledi, B. Terschanski, S. Elgeti, J. Kowalski, A level-set based space-time finite element approach to the modelling of solidification and melting processes, *Journal of Computational Physics* 457 (2022) 111047. arXiv:2105.09286, doi:10.1016/j.jcp.2022.111047.
URL <https://doi.org/10.1016/j.jcp.2022.111047>
- [24] A. Limare, S. Popinet, C. Josserand, Z. Xue, A. Ghigo, A hybrid level-set / embedded boundary method applied to solidification-melt problems, *Journal of Computational Physics* 474 (2023) 111829. arXiv:2202.08300, doi:10.1016/j.jcp.2022.111829.
URL <http://arxiv.org/abs/2202.08300><https://linkinghub.elsevier.com/retrieve/pii/S0021999122008920>
- [25] R. Scardovelli, S. Zaleski, DIRECT NUMERICAL SIMULATION OF FREE-SURFACE AND INTERFACIAL FLOW, *Annual Review of Fluid Mechanics* 31 (1) (1999) 567–603. doi:10.1146/annurev.fluid.31.1.567.
URL <https://www.annualreviews.org/doi/10.1146/annurev.fluid.31.1.567>
- [26] C. Hirt, B. Nichols, Volume of fluid (VOF) method for the dynamics of free boundaries, *Journal of Computational Physics* 39 (1) (1981) 201–225. doi:10.1016/0021-9991(81)90145-5.
URL <https://www.sciencedirect.com/science/article/pii/0021999181901455><https://linkinghub.elsevier.com/retrieve/pii/0021999181901455>
- [27] A. Karma, W. J. Rappel, Quantitative phase-field modeling of dendritic growth in two and three dimensions, *Physical Review E - Statistical Physics, Plasmas, Fluids, and Related Interdisciplinary Topics* 57 (4) (1998) 4323–4349. doi:10.1103/PhysRevE.57.4323.

- [28] H. Wang, R. Li, T. Tang, Efficient computation of dendritic growth with r-adaptive finite element methods, *Journal of Computational Physics* 227 (12) (2008) 5984–6000. doi:10.1016/j.jcp.2008.02.016.
- [29] X. Hu, R. Li, T. Tang, A multi-mesh adaptive finite element approximation to phase field models, *Communications in Computational Physics* 5 (5) (2009) 1012–1029.
- [30] J. Zhu, X. Chen, T. Y. Hou, An efficient boundary integral method for the Mullins-Sekerka problem, *Journal of Computational Physics* 127 (2) (1996) 246–267. doi:10.1006/jcph.1996.0173.
- [31] V. Cristini, J. Lowengrub, Three-dimensional crystal growth—I: linear analysis and self-similar evolution, *Journal of Crystal Growth* 240 (1-2) (2002) 267–276. doi:10.1016/S0022-0248(02)00831-X.
URL <https://linkinghub.elsevier.com/retrieve/pii/S002202480200831X>
- [32] V. Cristini, J. Lowengrub, Three-dimensional crystal growth - II: Nonlinear simulation and control of the Mullins-Sekerka instability, *Journal of Crystal Growth* 266 (4) (2004) 552–567. doi:10.1016/j.jcrysgro.2004.02.115.
- [33] C. S. Peskin, Numerical analysis of blood flow in the heart, *Journal of Computational Physics* 25 (3) (1977) 220–252. doi:10.1016/0021-9991(77)90100-0.
URL <https://linkinghub.elsevier.com/retrieve/pii/0021999177901000>
- [34] C. S. Peskin, The immersed boundary method, *Acta Numerica* 11 (2002) 479–517. doi:10.1017/S0962492902000077.
URL https://www.cambridge.org/core/product/identifier/S0962492902000077/type/journal_article
- [35] K. Taira, T. Colonius, The immersed boundary method: A projection approach, *Journal of Computational Physics* 225 (2) (2007) 2118–2137. doi:10.1016/j.jcp.2007.03.005.
- [36] R. J. Leveque, Z. Li, Immersed interface method for elliptic equations with discontinuous coefficients and singular sources, *SIAM Journal on Numerical Analysis* 31 (4) (1994) 1019–1044. doi:10.1137/0731054.
URL <https://doi.org/10.1137/0731054>
- [37] Z. Li, Immersed interface methods for moving interface problems, *Numerical Algorithms* 14 (4) (1997) 269–293. doi:10.1023/A:1019173215885.
URL <https://doi.org/10.1023/A:1019173215885>
- [38] R. J. LeVeque, Z. Li, Immersed Interface Methods for Stokes Flow with Elastic Boundaries or Surface Tension, *SIAM Journal on Scientific Computing* 18 (3) (1997) 709–735. doi:10.1137/S1064827595282532.
URL <http://epubs.siam.org/doi/10.1137/S1064827595282532>
- [39] Z. Li, M. C. Lai, The immersed interface method for the navier-stokes equations with singular forces, *Journal of Computational Physics* 171 (2) (2001) 822–842. doi:10.1006/jcph.2001.6813.
- [40] R. P. Fedkiw, T. Aslam, B. Merriman, S. Osher, A Non-oscillatory Eulerian Approach to Interfaces in Multimaterial Flows (the Ghost Fluid Method), *Journal of Computational Physics* 152 (2) (1999) 457–492. doi:10.1006/jcph.1999.6236.
- [41] R. P. Fedkiw, T. Aslam, S. Xu, The Ghost Fluid Method for Deflagration and Detonation Discontinuities, *Journal of Computational Physics* 154 (2) (1999) 393–427. doi:10.1006/jcph.1999.6320.
- [42] X. D. Liu, R. P. Fedkiw, M. Kang, A Boundary Condition Capturing Method for Poisson’s Equation on Irregular Domains, *Journal of Computational Physics* 160 (1) (2000) 151–178. doi:10.1006/jcph.2000.6444.
- [43] D. Q. Nguyen, R. P. Fedkiw, M. Kang, A boundary condition capturing method for incompressible flame discontinuities, *Journal of Computational Physics* 172 (1) (2001) 71–98. doi:10.1006/jcph.2001.6812.
- [44] H.-J. Jou, P. Leo, J. Lowengrub, Microstructural evolution in inhomogeneous elastic media, *Journal of Computational Physics* 131 (1997) 109–148. doi:10.1006/jcph.1996.5581.
URL <https://linkinghub.elsevier.com/retrieve/pii/S0021999196955813>
- [45] T. Y. Hou, Z. Shi, Removing the stiffness of elastic force from the immersed boundary method for the 2D Stokes equations, *Journal of Computational Physics* 227 (21) (2008) 9138–9169. arXiv:0801.2398, doi:10.1016/j.jcp.2008.03.002.
- [46] T. Y. Hou, Z. Shi, An efficient semi-implicit immersed boundary method for the Navier-Stokes equations, *Journal of Computational Physics* 227 (20) (2008) 8968–8991. doi:10.1016/j.jcp.2008.07.005.
- [47] V. Cristini, J. Lowengrub, Q. Nie, Nonlinear simulation of tumor growth, *Journal of Mathematical Biology* 46 (3) (2003) 191–224. doi:10.1007/s00285-002-0174-6.
URL <http://link.springer.com/10.1007/s00285-002-0174-6>
- [48] S. Li, J. S. Lowengrub, P. H. Leo, V. Cristini, Nonlinear theory of self-similar crystal growth and melting, *Journal of Crystal Growth* 267 (3-4) (2004) 703–713. doi:10.1016/j.jcrysgro.2004.04.002.
URL <https://linkinghub.elsevier.com/retrieve/pii/S0022024804004014>
- [49] S. Li, J. S. Lowengrub, P. H. Leo, V. Cristini, Nonlinear stability analysis of self-similar crystal growth: control of the Mullins-Sekerka instability, *Journal of Crystal Growth* 277 (1-4) (2005) 578–592. doi:10.1016/j.jcrysgro.2004.12.042.
URL <https://linkinghub.elsevier.com/retrieve/pii/S0022024804020196>

- [50] S. Li, J. S. Lowengrub, P. H. Leo, Nonlinear morphological control of growing crystals, *Physica D: Nonlinear Phenomena* 208 (3-4) (2005) 209–219. doi:10.1016/j.physd.2005.06.021.
URL <https://linkinghub.elsevier.com/retrieve/pii/S0167278905002691>
- [51] W. Ying, C. S. Henriquez, A kernel-free boundary integral method for elliptic boundary value problems, *Journal of Computational Physics* 227 (2) (2007) 1046–1074. doi:10.1016/j.jcp.2007.08.021.
URL <https://linkinghub.elsevier.com/retrieve/pii/S0021999107003774>
- [52] W. Ying, W. C. Wang, A kernel-free boundary integral method for implicitly defined surfaces, *Journal of Computational Physics* 252 (2013) 606–624. doi:10.1016/j.jcp.2013.06.019.
URL <http://dx.doi.org/10.1016/j.jcp.2013.06.019>
- [53] Y. Xie, W. Ying, A fourth-order kernel-free boundary integral method for implicitly defined surfaces in three space dimensions, *Journal of Computational Physics* 415 (2020) 109526. doi:10.1016/j.jcp.2020.109526.
URL <https://doi.org/10.1016/j.jcp.2020.109526>
- [54] W. Ying, W. C. Wang, A kernel-free boundary integral method for variable coefficients elliptic pdes, *Communications in Computational Physics* 15 (4) (2014) 1108–1140. doi:10.4208/cicp.170313.071113s.
- [55] R. Peyret, *Spectral Methods for Incompressible Viscous Flow*, Vol. 148 of Applied Mathematical Sciences, Springer New York, New York, NY, 2002, pp. XII, 434. doi:10.1007/978-1-4757-6557-1.
URL <http://link.springer.com/10.1007/978-1-4757-6557-1>
- [56] G. C. Hsiao, W. L. Wendland, *Boundary Integral Equations*, Springer International Publishing, Cham, 2021, pp. 25–94. doi:10.1007/978-3-030-71127-6_2.
URL https://doi.org/10.1007/978-3-030-71127-6_2
- [57] Y. Saad, *Iterative Methods for Sparse Linear Systems*, 2nd Edition, Society for Industrial and Applied Mathematics, 2003. doi:10.1137/1.9780898718003.
- [58] T. Beale, A. Layton, On the accuracy of finite difference methods for elliptic problems with interfaces, *Communications in Applied Mathematics and Computational Science* 1 (1) (2006) 91–119. doi:10.2140/camcos.2006.1.91.
URL <http://www.physics.nyu.edu/~simfh417/ensemble-sampler-with-affine-invariance.pdf>
<http://msp.org/camcos/2006/1-1/p05.xhtml>
- [59] A. Brandt, N. Dinar, Multigrid Solutions to Elliptic Flow Problems, in: S. V. PARTER (Ed.), *Numerical Methods for Partial Differential Equations*, Academic Press, 1979, pp. 53–147. doi:<https://doi.org/10.1016/B978-0-12-546050-7.50008-3>.
URL <https://www.sciencedirect.com/science/article/pii/B9780125460507500083>
- [60] A. Brandt, I. Yavneh, On multigrid solution of high-reynolds incompressible entering flows, *Journal of Computational Physics* 101 (1) (1992) 151–164. doi:[https://doi.org/10.1016/0021-9991\(92\)90049-5](https://doi.org/10.1016/0021-9991(92)90049-5).
URL <https://www.sciencedirect.com/science/article/pii/0021999192900495>
- [61] J. Prüss, G. Simonett, *Moving interfaces and quasilinear parabolic evolution equations*, Vol. 105, Springer, 2016.
- [62] K. Sakakibara, Y. Miyatake, A fully discrete curve-shortening polygonal evolution law for moving boundary problems, *Journal of Computational Physics* 424 (2021) 109857. doi:10.1016/j.jcp.2020.109857.
URL <https://doi.org/10.1016/j.jcp.2020.109857>
- [63] H. Chen, C. Min, F. Gibou, A numerical scheme for the stefan problem on adaptive cartesian grids with supralinear convergence rate, *Journal of Computational Physics* 228 (16) (2009) 5803–5818. doi:10.1016/j.jcp.2009.04.044.
- [64] H. Zhou, W. Ying, A Dimension Splitting Method for Time Dependent PDEs on Irregular Domains, *Journal of Scientific Computing* 94 (1) (2023) 20. doi:10.1007/s10915-022-02066-5.
URL <https://doi.org/10.1007/s10915-022-02066-5>
<https://link.springer.com/10.1007/s10915-022-02066-5>